

AD A 013220

NSWC/WOL/TR 75-53

12
45

NSWC/WOL/TR 75-53

NSWC

TECHNICAL REPORT

WHITE OAK LABORATORY

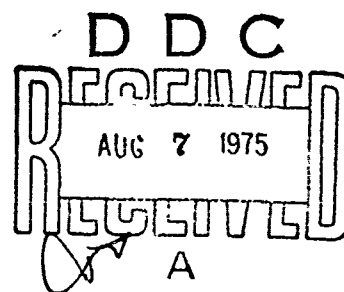
SHOCK-TUBE DIAGNOSTICS UTILIZING LASER RAMAN SPECTROSCOPY

BY
A.A. Boiarski

17 APRIL 1975

NAVAL SURFACE WEAPONS CENTER
WHITE OAK LABORATORY, SILVER SPRING, Md. 20910

- Approved for public release; distribution unlimited



NAVAL SURFACE WEAPONS CENTER
WHITE OAK, SILVER SPRING, MARYLAND 20910

ORDER FOR

WTIS White Series ☒
P.O. Ref Series ☐


UNCLASSIFIED

JUSTIFICATION

FY

DISTRIBUTION/AVAILABILITY CODES

DATE MAIL ETO/OF SPECIAL

		
---	--	--

Unclassified

SECURITY CLASSIFICATION OF THIS PAGE (When Data Entered)

REPORT DOCUMENTATION PAGE		READ INSTRUCTIONS BEFORE COMPLETING FORM
1. REPORT NUMBER 14 NSWC/WOL/TR-75-53	2. GOVT ACCESSION NO.	3. RECIPIENT'S CATALOG NUMBER 9
4. TITLE (and Subtitle) Shock-Tube Diagnostics Utilizing Laser Raman Spectroscopy		5. TYPE OF REPORT & PERIOD COVERED Technical Report
7. AUTHOR(s) 10 A. A. Boiarski		6. PERFORMING ORG. REPORT NUMBER
9. PERFORMING ORGANIZATION NAME AND ADDRESS Naval Surface Weapons Center White Oak Laboratory White Oak, Silver Spring, Maryland 20910		10. PROGRAM ELEMENT, PROJECT, TASK AREA & WORK UNIT NUMBERS SEA-18503/S1754
11. CONTROLLING OFFICE NAME AND ADDRESS		12. REPORT DATE 17 Apr 1975
		13. NUMBER OF PAGES 60
14. MONITORING AGENCY NAME & ADDRESS (if different from Controlling Office)		15. SECURITY CLASS. (of this report) Unclassified
		15a. DECLASSIFICATION/DOWNGRADING SCHEDULE
16. DISTRIBUTION STATEMENT (of this Report) Approved for public release; distribution unlimited.		
17. DISTRIBUTION STATEMENT (of the abstract entered in Block 20, if different from Report)		
18. SUPPLEMENTARY NOTES		
19. KEY WORDS (Continue on reverse side if necessary and identify by block number) Raman scattering Shock tube diagnostics Gas flow analysis Laser spectroscopy		
20. ABSTRACT (Continue on reverse side if necessary and identify by block number) The laser Raman scattering technique shows potential as a diagnostic method for determining the chemical and thermodynamic state of high-temperature gases. To investigate the utility of this technique for shock-tube diagnostics, and to validate the method at known elevated temperatures, vibrational Raman intensities were measured behind an incident shock wave. Intensity history data through the wave front,		

DD FORM 1 JAN 73 1473

EDITION OF 1 NOV 65 IS OBSOLETE
S/N 0102-014-66011

Unclassified

SECURITY CLASSIFICATION OF THIS PAGE (When Data Entered)

391596

Unclassified

SECURITY CLASSIFICATION OF THIS PAGE (When Data Entered)

vibrational excitation times of oxygen in air, along with temperature and density measurements for oxygen and nitrogen in air were obtained over a range of postshock conditions. The measured densities and temperatures were found to be in good agreement with shock-wave theory. An excitation time measurement also agreed well with shock-tube data obtained with other diagnostic methods. In general, the results indicated that the Raman scattering technique was accurate at elevated temperatures and should prove useful in determining the thermochemical state of gases in continuous flows as well as in shock tubes and other impulse facilities.

Unclassified

SECURITY CLASSIFICATION OF THIS PAGE (When Data Entered)

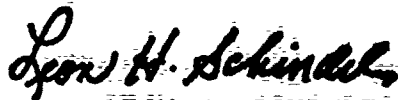
17 April 1975

SHOCK-TUBE DIAGNOSTICS UTILIZING LASER RAMAN SPECTROSCOPY

This report documents measurements of high temperature gas properties behind a shock wave utilizing the laser Raman scattering, LRS, technique. The data was obtained at known postshock conditions in order to calibrate the experimental equipment for gasdynamic laser cavity diagnostics which were to follow. Since the IRS method is not as well known as other measurement techniques, a rather complete description of the required spectroscopic theory is also presented.

This work was supported by the Naval Sea Systems Command under Task No. SEA 18503/S1754.

The author wishes to thank Mr. J. L. Wagner for his assistance in setting up the shock tube and Messrs. J. Janzegers, S. A. Longas and B. J. Crapo for their help during installation of experimental hardware and electronic instrumentation.



LEON H. SCHINDEL
By direction

CONTENTS

	Page
I. INTRODUCTION.....	1
II. DETERMINATION OF THE THERMOCHEMICAL STATE OF A SHOCK HEATED GAS.....	3
A. GENERAL DISCUSSION.....	3
B. ROTATION-VIBRATION LINE INTENSITIES.....	4
C. TEMPERATURE DETERMINATION.....	8
D. NUMBER DENSITY MEASUREMENT.....	11
E. RATE MEASUREMENTS.....	12
1. Vibration Excitation Time.....	12
2. Chemical Reaction Time.....	13
III. SHOCK TUBE IN RAMAN SCATTERING EXPERIMENTS.....	14
A. GENERAL DISCUSSION.....	14
B. BRIEF DESCRIPTION OF FACILITY.....	14
C. POSTSHOCK PROPERTIES.....	15
IV. RAMAN INSTRUMENTATION FOR SHOCK TUBE DIAGNOSTICS...	16
A. GENERAL DISCUSSION.....	16
B. OVERALL EXPERIMENTAL SETUP.....	16
C. ELECTRO-OPTICAL COMPONENTS.....	17
D. COINCIDENCE TIMING.....	18
V. SHOCK TUBE RAMAN DATA.....	20
A. TIME HISTORY OF SCATTERING INTENSITY.....	20
B. DETERMINATION OF VIBRATIONAL EXCITATION TIME FOR OXYGEN IN AIR.....	21
C. TEMPERATURE AND DENSITY DETERMINATION USING SPECTRAL SCAN METHOD.....	23
D. TEMPERATURE AND DENSITY MEASUREMENT USING 2-COLOR TECHNIQUE.....	28

CONTENTS (Cont.)

	Page
VI. DISCUSSION OF RESULTS.....	31
VII. CONCLUSIONS.....	34

ILLUSTRATIONS

Figure	Title
1	Calculated Rotation-Vibration Even J, Q-Branch Line Intensities and Frequency Shifts for Molecular Nitrogen at 300°K and 1000°K
2	Unresolved Stokes Rotation-Vibration Spectra of Nitrogen at $T_V=T_R=300^\circ\text{K}$ and 3000°K Computed for Narrow Triangular Apparatus Function
3	Unresolved Stokes Rotation-Vibration Spectra of Oxygen at $T_V=T_R=300^\circ\text{K}$, 900°K and 1500°K Computed for the Broad Experimental Apparatus Function
4	Unresolved Stokes Rotation Vibration Spectra of Oxygen for Nonequilibrium Conditions Behind an Incident Shock Wave for $T_V<T_R=1100^\circ\text{K}$
5	Schematic of Raman Scattering Apparatus for Shock-Tube Experiment
6	Raman Setup for Shock-Tube Experiment Emphasizing Laser Beam Path
7	Entire Raman Setup for Shock-Tube Experiment
8	Schematic of Electro-Optical Components of Data Gathering System
9	Oscilloscope Trace of Raman and Laser Output (N_2 in air- $p_{\text{AIR}}=200$ Torr, $\lambda_A=8283\text{\AA}$)
10	Timing Circuitry for Raman Shock-Tube Experiment
11	Time History of Raman Scattering in a Shock-Tube Experiment
12	Density Ratio as a Function of Time Behind the Wave Front
13	Time History of Raman Scattering from Oxygen Behind a Shock Wave in Air
14	Raw Data for Scan Method of Determining Density and Temperature Using LRS
15	Reduced Data for Scan Method of Determining Temperature and Density Using LRS

ILLUSTRATIONS (Cont.)

Figure	Title
16	Theoretical Curve Used to Obtain Temperature Correction for Density Determination
17	Raw Data for 2-Color Method of Determining Density and Temperature Using LRS
18	Reduced Data for 2-Color Method of Determining Temperature and Density Using LRS
19	Theoretical Curves Used to Obtain N_2 Temperature and Temperature Correction for Density Determination
20	Comparison of a Raman O_2 in Air V-T Excitation Time Measurement With Other Shock-Tube Data
21	Raman Temperature Ratio Measurements Compared to Theory for O_2 and N_2 in Shock-Heated Air
22	Raman Density Ratio Measurements Compared to Theory For O_2 and N_2 in Shock-Heated Air

SYMBOLS

$A(\Delta\lambda)$	apparatus function
B_e	rotational constant, cm^{-1}
B_v	rotational constant for vth vibrational state, cm^{-1}
c	velocity of light, cm/sec
D_e	rotational constant, cm^{-1}
D_v	rotational constant for vth vibrational state, cm^{-1}
E	energy, joules
ΔE	quantized energy change, joules
$F(J)$	rotational term value, cm^{-1}
$G(v)$	vibrational term value, cm^{-1}
g_J	spin degeneracy factor
h	Plancks' constant, joule-sec
I	Raman intensity
\bar{I}	normalized Raman intensity
I_B	background light intensity
I_L	arbitrary value of incident laser intensity
I_R	arbitrary value of measured Raman intensity
$I_R(\lambda)$	computed Raman intensity
J	rotational quantum number
ΔJ	change in J during Raman transition
K	cross section constant

l	scattering volume length, cm
N_0	incident photon flux, sec^{-1}
$N_{v,J}$	theoretical Raman line intensity, sec^{-1}
N_{λ}	computed Raman intensity flux, sec^{-1}
n^p	gas number density, cm^{-3}
p	gas pressure, torr or atm
p_1	preshock gas pressure, torr
Q	state sum
S_J	rotational line strength factor
S_v	vibrational band strength factor
T	temperature, $^{\circ}\text{K}$
t	time, sec
v	vibrational quantum number
Δv	change in v during Raman transition
W_s	shock speed, meters/sec
α_e	rotational constant, cm^{-1}
β_e	rotational constant, cm^{-1}
γ	ratio of specific heats
Δ	wavelength correction factor, \AA
η_i	mole fraction of species i
λ	wavelength, \AA
ν_0	incident laser frequency, cm^{-1}
ν	frequency, cm^{-1}
$\Delta\nu_{v,J}$	frequency shift, cm^{-1}
ρ	gas density, grams/cm^3
$\sigma_{v,J}$	scattering cross section, $\text{cm}^2/\text{particle-sr}$

τ	excitation time, sec
Ω	solid angle of collection optics, steradians
ω_e	vibrational constant, cm^{-1}
$\omega_e x_e$	vibrational constant, cm^{-1}
$\omega_e y_e$	vibrational constant, cm^{-1}
$\chi_{v,J}$	related to population density

Subscripts

A	actual value
C, Calib.	calibration condition
D	delay
F.L.	laser flash lamp
I	indicated value
J	rotational state
L	laser value
Lab	laboratory fixed coordinates
m	molecular property
max	maximum intensity
o	incident laser value
p	peak value
Q.S.	laser Q-switch
R	Raman value
S	scan value
rot, r	rotational energy mode
STD	standard condition
T	theoretical value
V-T	vibration-translation energy exchange process

NSWC/WOL/TR 75-53

vib, v	vibrational energy mode
w	wave fixed coordinates
1	preshock, also integer label
2	postshock, also integer label
4	driver gas property

I. INTRODUCTION

The development of non-perturbing optical gas diagnostic techniques has received much attention in the past few years. This renewed interest is mainly due to the advent of modern high powered lasers and their associated electro-optical equipment. One such diagnostic method of current interest is the laser Raman scattering (LRS) technique.

Several experiments have been reported in which the LRS method was used to determine the thermochemical state of a test gas. The number density of various species was measured at low temperatures in both static and flowing gases.¹⁻³ High temperature Raman scattering measurements were also obtained for temperatures near 1700°K in H₂/O₂-air flames.⁴ Several practical applications of LRS include the measurement of N₂ Raman scattering in an arc-heated wind tunnel environment⁵ and pollutant density measurements in a gas turbine exhaust.⁶

¹Hartley, D., "Transient Gas Concentration Measurements Utilizing Laser Raman Spectroscopy," AIAA Journal 10, pp. 687-689, May 1972

²Kellam, J. M. and Glick, M. M., "Gas Density Measurements in a Jet Using Raman Scattering," AIAA Journal 10, pp. 1389-1391, October 1972

³Widhopf, G. F. and Lederman, S., "Specie Concentration Measurements Utilizing Raman Scattering of a Laser Beam," AIAA Journal 9, pp. 309-316, February 1971

⁴Lapp, M., Goldman, L. M. and Penney, G. M., "Raman Scattering from Flames," Science 175, pp. 1112-1115, March 1972

⁵Boiarski, A. A. and Daum, F. L., "An Application of Laser-Raman-Spectroscopy to Thermochemical Measurements in an Arc Heated Wind Tunnel Flow," Aerospace Research Lab. Report ARL 72-0126, December 1972

⁶Bresowar, G. E. and Leonard, D. A., "Measurement of Gas Turbine Exhaust Pollutants by Raman Spectroscopy," AIAA/SAE 9th Propulsion Conference Paper No. 73-1276, Las Vegas, Nevada, 5-7 November 1973

The success of these experiments has prompted interest in the application of LRS as a diagnostic tool for shock tube research. White⁷ suggested using Raman scattering as a possible means of making a noninterfering point measurement of vibrational and/or rotational temperatures behind an incident shock wave. He concluded that the species concentrations of individual components in a gas mixture could be measured. Also, these species measurements, as well as energy mode population measurements, could be made whether or not thermochemical equilibrium existed.

An attempt was made by Milling⁸ to use Raman scattering as a diagnostic tool for measuring CO₂ dissociation rates in a shock tube experiment. No results were obtained, however, due to the fact that the CO₂ scattering cross section which he assumed was a factor of approximately ten times greater than a more recent measurement indicates.⁹

It was the objective of the present study to observe Raman scattering from high temperature O₂ and N₂ behind an incident shock wave in air. The postshock gas temperature and density were determined from the Raman technique and compared with known shock tube values over a relatively wide range of conditions. Besides this valuable high temperature calibration, the experiment also investigated the applicability of the LRS technique to shock tube excitation time measurements and general high temperature gas diagnostics.

⁷White, D. R., "Shock Tube Studies of Nitrogen Vibrational Relaxation and Methane Oxidation," Aerospace Research Lab. Report ARL 70-0107, June 1970

⁸Milling, R. W., "Use of Time Resolved Raman Scattering for the Measurement of Dissociation Rates in a Shock Tube," Seiler Research Lab. Report SRL 69-005, June 1969

⁹Penney, C. M., Goldman, L. M. and Lapp, M., "Raman Scattering Cross Sections," Nature Physical Science 235, No. 58, pp. 110-112, 7 February 1972

II. DETERMINATION OF THE THERMOCHEMICAL STATE OF A SHOCK HEATED GAS

A. GENERAL DISCUSSION

When light passes through a gas, weak randomly directed radiation at the same frequency will appear due to scattering of the light by the gas molecules. The blue of the sky represents such an effect. In 1928 Raman¹⁰ observed the spectrum of the light scattered from many different gases and liquids. Using a monochromatic source of frequency, ν_0 , he noted that the scattered light not only contained this incident frequency (i.e., Rayleigh scattering) but also several shifted frequencies, $\nu_0 - \nu_1$, $\nu_0 - \nu_2$, and others, $\nu_0 + \nu_1$ and $\nu_0 + \nu_2$. It was found that ν_1 and ν_2 were frequencies which were characteristic of the scattering molecule. That is, for a particular molecule, the shifted frequencies were different than frequencies obtained for any other molecule. This frequency shift phenomenon became known as the Raman effect. The radiation shifted toward lower frequencies is called "Stokes" radiation and the weaker radiation at higher frequencies, "anti-Stokes." Since its discovery, the Raman scattering effect has been examined for many different molecules and has been an important tool used by physicists for studying molecular structure at known densities and temperatures.

The Raman phenomena can be qualitatively explained by considering the molecule-photon interaction from the standpoint of conservation of energy. The incident photon at frequency ν_0 and energy $E_0 = h\nu_0$ interacts with a molecule having energy E_m . This inelastic interaction produces a scattered photon of a different energy, $E_{\text{Raman}} = h\nu_{\text{Raman}}$, at a shifted frequency ν_{Raman} . The energy differential is accounted for through a gain or loss of energy by the molecule. Since the molecular energy is quantized, only discrete amounts of energy may be exchanged in the interaction. Hence, the molecule must have an energy E_m' after the interaction which differs from its initial energy by a specified amount $\Delta E_{\text{rot-vib}}$. This energy differential is a known function of the bound energy states of the particular scattering molecule. Balancing energy before and after the interaction, the photon energies (i.e., frequencies) observed in Raman scattering must then correspond to the photon energy of the incident radiation shifted by an amount which is characteristic of the scattering molecule.

¹⁰Raman, C. V., Indian Journal Physics 2, p. 287, 1928

The amount of frequency shift is given by:

$$\nu_0 \pm \nu_{\text{Raman}} = \frac{\Delta E_{\text{rot-vib}}}{hc} \quad (1)$$

At first there seems to be a myriad of possibilities for the scattered photon frequencies due to the many possible molecular vibrational energy states, denoted by quantum number v , each having many associated rotational energy levels, denoted by the quantum number J . However, there are selection rules which govern molecular energy transitions that can occur between various energy levels. The selection rules for a diatomic molecule undergoing Raman transitions are:

$$\Delta v = 0, \pm 1 \text{ (for vibrational transitions)}$$

and

(2)

$$\Delta J = 0, \pm 2 \text{ (for rotational transitions)}$$

These selection rules limit the number of allowed frequency shifts tremendously. However, in this study even fewer transitions will be investigated since only the $\Delta v = +1$ vibrational and $\Delta J = 0$ rotational transitions are important. These transitions give rise to the so-called Stokes vibration-rotation Q-branch Raman effect.

Even with the above restrictions, many transitions are still possible. This becomes evident, for example, when considering the Stokes Q-branch $v=0$ to $v=1$ vibrational transition, where $J=1$ to $J=1$, $J=2$ to $J=2$, etc. rotational transitions can occur as well as the $J=0$ to $J=0$. Due to small differences in rotational energy level spacing, the resulting frequencies are quite close but distinguishable. Also, $v=1$ to $v=2$, $v=2$ to $v=3$, etc. vibrational Q-branch transitions can occur with all the $\Delta J = 0$ transitions included in each $\Delta v = 1$ vibrational transition. The various vibrational transitions are easily distinguished due to molecular anharmonicity. Hence, 1000-2000 Raman Q-branch transitions may be considered in the analysis of the Stokes rotation-vibration spectrum.

B. ROTATION-VIBRATION LINE INTENSITIES

Smekal¹¹ predicted the Raman effect in 1923 and since that time the theory of Raman scattering has become well developed from both

¹¹Smekal, A., "Zur Quantentheorie der Dispersion," Naturwiss 11, p. 873, September 1923

the quantum mechanical and the semi-classical viewpoints.^{12,13} Hence, only the results of the detailed theoretical investigations will be presented in this report.

The observed Raman intensity flux in photons/second, resulting from a particular Stokes rotation-vibration transition is given by:

$$N_{v,J} = N_0 \chi_{v,J} \sigma_{v,J} \Omega \ell n \quad (4)$$

where N_0 is the number of incident photons/second, ℓ is the optically observed length of the laser beam in centimeters, Ω is the solid angle of the collection optics in steradians, n is the number of molecules per cubic cm in the gas sample and $\chi_{v,J}$ is related to the fraction of molecules in energy state $E_{v,J}$. Equation (4) shows that collected intensities vary directly with the incident photon flux. This fact explains why the advent of modern high intensity lasers has increased interest in Raman scattering as a practical diagnostic technique. Also, the Raman intensity is directly proportional to gas number density so measurements can be used to determine unknown density conditions.

Further examination of Equation (4) shows that the collected intensity is directly related to several experimental factors, namely, collector solid angle and observed laser beam length. Since the Raman photon flux is scattered nearly uniformly into 4π steradians, a larger collector implies a greater collection efficiency. The scattering volume (i.e., volume from which collected photons originate) is defined by the laser beam cross section dimensions and the field of view of the optics. The volume varies linearly with the square of beam diameter and observed beam length. This is an important aspect of the Raman technique since it indicates that the measurement is truly a point determination of gas properties within the scattering volume. By focusing the laser beam and using optical stops to obtain a small observed length, the spatial resolution can be improved. However, Raman signal intensity is sacrificed when smaller and smaller field stops are employed.

Finally, the relation of the Raman scattering intensity to energy state population implies that detailed information can be obtained on population distributions in a gas. For non-Boltzmann conditions such as would exist in a laser cavity, a population distribution measurement is important. However, when Boltzmann statistics prevail, determination of the temperatures of various molecular modes is critical.

¹²Kramers, H. A. and Heisenberg, W., "Über die Streuung von Strahlung durch Atome," Z. Physik 31, p. 681, January 1925

¹³Placzek, G., "The Rayleigh and Raman Scattering," UCLR-Trans-526(L), translated from a publication of the Akademische Verlagsgesellschaft G.M.B.H., Leipzig, 1934

The symbol $\sigma_{v,J}$ in Eq. (4) is the scattering cross section (i.e., $\text{cm}^2/\text{particle-sr}$) or transition probability for the particular $v \rightarrow v+1$, $J \rightarrow J$ transition and is written as:

$$\sigma_{v,J} = K (\nu_0 - \Delta\nu_{v,J})^4 g_J S_v \quad (5)$$

where K is a constant which can be theoretically estimated and experimentally measured. The frequency shift $\Delta\nu_{v,J}$ of a Stokes Raman Q-branch line which appears in Eq. (5) is given by Reference 14 as:¹⁴

$$\Delta\nu_{v,J}^Q = \Delta\nu_v - \alpha_e J(J+1) - \beta_e J^2(J+1)^2 \quad (6)$$

where:

$$\Delta\nu_v = \omega_e - 2\omega_e x_e(v+1) + \omega_e y_e(3v^2 + 6v + 13/4) \quad (7)$$

In Equations (6) and (7) above, ω_e , $\omega_e x_e$ and $\omega_e y_e$ are vibrational constants and α_e , β_e , are rotational constants of the scattering molecule. The values of the above parameters used in the calculations reported in this text were taken from Reference 14. The symbol g_J in Eq. (5) is the spin degeneracy factor, which depends on the symmetry properties of a particular molecule and whether J is an even or odd integer. S_v , the vibrational band-strength factor, is given by:

$$S_v = v+1 \quad (8)$$

From Eq. (8), it can be seen that a $v=1$ to $v=2$ transition has twice the probability of occurring than the $v=0$ to $v=1$. For a Boltzmann population distribution, $\chi_{v,J}$ is a function of the vibrational temperature T_v and the rotational temperature T_r of the scattering molecule and is written:

$$\chi_{v,J} = \frac{S_J e^{-\frac{1.44F(J)}{T_r}} e^{-\frac{1.44G(v)}{T_v}}}{Q_{\text{rot}} Q_{\text{vib}}} \quad (9)$$

¹⁴ Herzberg, G., Spectra of Diatomic Molecules, D. van Nostrand Company, Inc., New York, pp. 552-561, 1950

where the state sums Q_{rot} and Q_{vib} are given as:

$$Q_{\text{rot}} = \sum_J (2J+1) e^{-\frac{1.44F(J)}{T_r}} \quad (9)$$

$$Q_{\text{vib}} = \sum_v e^{-\frac{1.44G(v)}{T_v}}$$

The functions $F(J)$ and $G(v)$ which appear in Eq. (9) are so-called term values and are written as:

$$F(J) = B_v J(J+1) - D_v J^2 (J+1)^2 \quad (10)$$

and

$$G(v) = \omega_e (v+1/2) - \omega_e x_e (v+1/2)^2 + \omega_e y_e (v+1/2)^3$$

In Eq. (9) S_J is the line strength factor for Q-branch transitions and is given by:

$$S_J = (2J+1) \quad J=0,1,2,\dots \quad (11)$$

In Eq. (10) B_v and D_v are written as:

$$B_v = B_e - \alpha_e (v+1/2) \quad (12)$$

$$D_v = D_e + \beta_e (v+1/2)$$

Again B_e and D_e are rotational constants of the scattering molecule (Ref. 14).

The above equations show that the Raman line intensities are complex functions of number density, rotational temperature, vibrational temperature and various molecular constants and known experimental factors. Further, Raman frequency shifts are uniquely dependent on the scattering molecule. Hence, a measurement of the frequency

spectrum can yield an identification of the molecules which are present in the test sample. Also, the concentration of each constituent and the rotational and vibrational temperatures of each molecule species can be determined from a spectral intensity analysis.

C. TEMPERATURE DETERMINATION

In the above equations the Raman spectrum (i.e., $N_{v,J}$ vs. $\Delta v_{v,J}$) was shown to be a function of the rotational and vibrational population distributions of the molecules in a gas. For Boltzmann population conditions, the equations imply that a measurement of the spectrum would yield information concerning the rotational and vibrational temperatures independently. Hence, thermodynamic non-equilibrium conditions (i.e., $T_v \neq T_r$) could be investigated. The above statements come as no great surprise to one versed in other spectroscopic techniques, for the power of spectroscopy has been its ability to determine detailed thermochemical information about molecules in a test gas. The following describes how Raman spectroscopic information can be utilized in this respect.

From the above equations, the temperature dependence of the Q-branch Raman rotation-vibrational lines of molecular nitrogen was calculated for illustrative purposes. The results for the even rotational lines at $T_v = T_r = 300^\circ\text{K}$ and 1000°K are plotted in Figure 1. A shift in the peak rotational intensity within the (0,1) rotation-vibration band at 2300 cm^{-1} occurs as the temperature increases. This so-called "blue shift" is due to the increase in population of the upper rotational states with increasing rotation temperature. Also, at 1000°K a small set of frequency shifts appear at about 2300 cm^{-1} resulting from the ($v=1 \rightarrow v=2$) or (1,2) Q-branch transitions. These upper state Raman transitions appear in the spectrum due to the increase in the population of the upper vibrational states with increasing vibrational temperature.

In practice, a spectrum such as that shown in Figure 1 would be difficult to obtain due to the high resolution required to give individual rotational line intensities and due to the overlap of rotational lines of adjacent Q-branches. Hence, resolved spectra will not normally be obtained experimentally. To compute the unresolved spectrum, the Raman line intensities given above must be convoluted with the apparatus function $A(\Delta\lambda)$ of the measuring instrument since more than one Raman line will be transmitted by the device. The apparatus function, with a peak transmission at wavelength λ_p , may then be scanned through the spectrum. The unresolved spectral intensity N_{λ_p} is then given by:

$$N_{\lambda_p} = \sum_{v,J} N_{v,J} A(\Delta\lambda) \quad (13)$$

and

$$\Delta\lambda = \lambda_p - \lambda_{v,J} \quad (13)$$

where

$$\lambda_{v,J} = \frac{10^8}{\nu_0 - \Delta\nu_{v,J}}$$

$N_{v,J}$ and $\Delta\nu_{v,J}$ are the Raman line intensities and frequency shifts, respectively, given by the detailed equations in the previous section. By varying λ_p through the region of the Raman lines, the unresolved spectral scan can be determined theoretically using a digital computer program to perform the straightforward but tedious computations. The computer code does nothing more than take each of the few thousand Raman line intensities and sum the product of these intensities and the apparatus function transmission values at the Raman wavelength of the particular transition. Each sum corresponds to a particular wavelength position of the peak of the apparatus function (or transmission curve if you will). The computer then increments this peak wavelength by a specified amount and repeats the entire procedure again and again until a theoretical wavelength scan is produced. Most of the Raman lines will not add to the sum of a narrow apparatus function because the transmission is zero at their particular wavelength, also when λ_p is outside the range of the larger Raman intensities, the sum will be negligible even at the peak transmission of the apparatus function. An example of such a calculation for molecular nitrogen at a constant number density and temperatures of 300°K and 3000°K is shown in Figure 2 for a ruby laser source where $\lambda_0 = 6943\text{\AA}$. A narrow 5\text{\AA} half-width triangular apparatus function was assumed. Note that individual rotational lines are not detectable as in Figure 1 since the apparatus function is wide enough to include many lines at once. However, the various Q-branches are able to be resolved with this particular apparatus function. Also, note the vast difference in the spectra at the two temperatures shown in Figure 2. At 300°K the Raman spectrum is limited to a narrow region of the total spectrum while at 3000°K a much broader wavelength interval is covered.

Since most early Raman work was done at room temperature or below, the term Raman "line" was adopted, because the Raman spectrum looked like a "line" (e.g., see Figure 2). However, approximately 20 actual rotational lines make up the Q-branch spectrum at room temperature, as shown in Figure 1; and, therefore, the term "line" is incorrect. At higher temperatures, where other Q-branches appear due to upper level vibrational transitions, the term "line" becomes

meaningless as well as incorrect. Therefore, a better term would be Raman "rotation-vibration spectrum" or just "Raman spectrum," which has been adopted in this report.

The apparatus function used in the calculations plotted in Figure 2 was somewhat narrow for the spectral analyzer used in this study. Therefore, the actual apparatus function employed in the present experiment was used to compute the unresolved Raman spectrum. The results of these calculations are shown in Figure 3 for oxygen at temperatures of $T_v = T_r = 300, 900$ and 1500°K . Note that the various Q-branches are not resolved for this relatively broad apparatus function, yet the spectral intensity profile is quite sensitive to gas temperature.

For a particular $\Delta v=1$ transition (i.e., (0,1) O-branch), Eq. (4) can be written:

$$\frac{N_{0,J}}{N_{0,0}} = \left[\frac{\nu_0 - \Delta\nu_{0,J}}{\nu_0 - \Delta\nu_{0,0}} \right]^4 \frac{S_J g_J}{S_0 g_0} e^{-\frac{1.44 F(J)}{T_r}} \quad (14)$$

Thus, the relative line intensity distribution in a given O-branch is a function only of the rotational temperature of the gas. This can be readily observed in Figures 1 and 2, where the wavelength of peak intensity in the (0,1) Q-branch has shifted toward the blue end of the spectrum at the higher temperature condition. Also, note that the asymmetry of the spectral profile is quite different for the elevated temperature case. Thus, by curve fitting the spectral profile of the (0,1) Q-branch and/or any other branch, the rotational temperature of the gas can be obtained from the rotation-vibration spectrum. Since the branches must be resolved, the narrower apparatus function, such as that used in Figure 2, must be used in order to obtain information on the rotational state of the scattering molecules.

Summing Eq. (4) over the rotational quantum number J will result in the following expression:

$$\frac{N_v}{N_0} = \left[\frac{\nu_0 - \Delta\nu_v}{\nu_0 - \Delta\nu_0} \right]^4 S_v e^{-\frac{1.44 G(v)}{T_v}} \quad (15)$$

where

$$\Delta\nu_v = \omega_e - 2\omega_e x_e(v+1) + \omega_e y_e(3v^2 + 6v + 13/4) \quad (16)$$

Hence, the relative integrated intensity of the branches is indicative of the vibrational state of the gas. In other words, the shape of each branch is a function of the rotational temperature, but the relative intensity of the various branches is dependent only on the vibrational temperature of the scattering molecules. It must be pointed out that, in general, accurate integrated Q-branch intensities are difficult to obtain due to the overlap of the various branches. Thus, Eq. (14) cannot be used in most cases to calculate the vibrational temperature from the unresolved spectrum. Instead, curve fitting techniques must be employed to obtain the vibrational temperature of the gas. Note that both of the above spectral analysis methods require only relative intensity measurements; no absolute intensities are needed.

For equilibrium conditions (i.e., $T_v = T_r = T$), a curve fit of the entire spectral intensity profile can be used to obtain the gas temperature. Either narrow or broad apparatus functions as in Figure 2 or Figure 3 can be used. However, if thermodynamic nonequilibrium is suspected, a separate curve fit must be made of one or more Q-branches to determine the rotational temperatures independently of the vibrational state of the gas. Then, the vibrational temperature can be determined from a curve fit of the entire rotation-vibration spectrum. The rotational temperature of the gas can be used as data for this calculation. Note, that narrow apparatus functions, as in Figure 2, must be used for the nonequilibrium case in order to determine independently the rotational and vibrational states of the test gas.

D. NUMBER DENSITY MEASUREMENT

A cursory examination of Eq. (4) might imply that the Raman spectrum could be used directly to evaluate the number density, n , of a gas under varying temperature conditions. This is not true since Raman line intensities are dependent upon temperature and number densities simultaneously. This coupling of number density and temperature is common to all spectroscopic techniques and arises from temperature effects on the population distribution of the various energy modes. The coupling effect can be readily demonstrated by considering the spectral plot shown in Figure 2, where constant number density was used in the calculations. Note that if the (0,1) Q-branch peak intensity were to be used to compute number density at 3000°K without making a correction for temperature effects, the calculated values, compared to room conditions, would be in error by a factor of about 5. Hence, the gas temperature must be known in order to obtain the correct number density of any of the species in the test gas. A temperature determination is, however, not dependent on knowledge of the actual density. For nonequilibrium conditions, both the vibrational and rotational temperatures must be obtained in order to correct for temperature dependence. This temperature effect on number density measurements can be minimized under certain circumstances. Note that by using a broader apparatus function, as shown in Figure 3, the resulting oxygen Raman spectrum

is nearly temperature independent at 7778\AA . Hence, by choosing proper experimental conditions the need for temperature corrections can be eliminated if a certain amount of calculable error is tolerable. In this case, the intensity of the oxygen Raman spectrum at 7778\AA is nearly directly proportional to the number density of oxygen for the particular apparatus function used in the calculations. Varying the shape of the apparatus function will change the optimum wavelength and also the error estimates.

To determine the number density of the constituents of high temperature air, the measurement of absolute spectral intensities is not required. Those difficult absolute measurements may be avoided through the application of a calibration point which is the known composition and number density of room air existing before and/or after the high temperature test condition. Also, the number density of any species which is present only in the test environment can be determined by ratioing its intensity value to a room temperature constituent such as nitrogen. Of course the nitrogen would also have to be present in the test environment. This is an attractive feature of the Raman scattering diagnostic method over other spectroscopic techniques which require either absolute intensity measurements or complex calibration procedures.

E. RATE MEASUREMENTS

1. Vibrational Excitation Time

A finite time is required for the vibrational temperature to equilibrate with temperatures of the rotational and translational modes of motion during rapid changes in molecular energy. This nonequilibrium process can be investigated using Raman scattering. To monitor both the vibrational and rotational temperature would be straightforward but cumbersome. A narrow apparatus function must be used, as discussed above, and data must be simultaneously obtained from at least three different wavelength positions requiring a good deal of instrumentation.

This type of temperature data would be informative; however, often only the time for the vibrational mode to equilibrate (i.e., vibrational-excitation time or τ_{v-T}) is of primary interest. A simple method can be used to determine τ_{v-T} utilizing Raman spectroscopy by monitoring the Raman intensity using a single spectrum analyzer. In this case, the transmission peak of the apparatus must be located at the proper wavelength position in the spectrum. Raman intensity calculations were performed for oxygen using Eq. (13) and assuming an abrupt change in the rotational temperature from ambient conditions to a value of 1100°K , due to the passage of a shock wave. The vibrational temperature was then theoretically increased from 300°K to 1100°K (i.e., from ambient to equilibration with the rotational temperature) as occurs behind the wave during vibration excitation. Results of these calculations are shown in Figure 4. Note that there is a significant change in the spectrum with just the rotational mode excited. Then the spectrum changes further as the population

of the upper vibrational state increases. Hence, τ_{V-T} is the time between the first change just behind the wave and the attainment of a constant value of the Raman intensity at thermodynamic equilibrium. Note that in Figure 4 the broad 22.5Å apparatus function is sufficient for these excitation time experiments.

2. Chemical Reaction Time

As with the internal modes of motion, chemical reactions also take a finite time to occur. Usually the excitation time for the internal modes is much shorter than reaction times so coupling can often be neglected. Measurement of the chemical reaction rate using Raman scattering involves monitoring the formation or consumption of a particular constituent with time. However, for a pure gas the chemical reaction process alters the heat content which results in a temperature change during the reaction. As discussed in Section D, spectroscopic intensities are functions of temperature as well as density. Hence, errors could be introduced into the rate measurements if this temperature-density coupling is not taken into account.

Again, one may monitor both the temperature and density. Thus, Raman intensity data would have to be obtained simultaneously for at least two different wavelength positions. The measured temperature could then be used to obtain corrected density histories from which chemical rates could be computed. A simpler way which avoids the temperature-density coupling would involve diluting the chemical reactants in a buffer gas such as argon. The chemical reaction would result in a negligible change in the total gas energy so the temperature would remain nearly constant. Now, a single measuring instrument (i.e., one broad apparatus function) could be used to directly monitor density changes with time. Chemical reaction rates could then be calculated without any error introduced by the need to measure temperature.

III. SHOCK TUBE IN RAMAN SCATTERING EXPERIMENTS

A. GENERAL DISCUSSION

The shock tube is essentially a device in which a planar shock wave is generated by the sudden bursting of a diaphragm which separates a high-pressure low molecular weight gas from a test gas at low pressure. Behind this wave the experimental gas is brought almost instantly to a known and controlled high temperature, held at steady temperature and pressure for a few hundred microseconds, and then cooled suddenly. If the gas is studied at some point along the tube, then it is possible to follow the progress of chemical reactions, and vibrational excitation processes as the sample of heated gas passes the measurement point. Since the density of the gas behind the wave is usually quite high, then Raman scattering measurements are facilitated by the increase in scattering intensity. The generation of a known thermochemical state of high density gas implies that the shock tube is a valuable tool for calibrating Raman measurement apparatus and validating Raman theory at elevated temperature conditions.

B. BRIEF DESCRIPTION OF FACILITY

To generate the temperature and density conditions necessary for this study, a 25 mm I.D. 3.5 meter long shock tube was used. The driver was operated with helium while the driven tube contained either pure nitrogen or dry air. Scored aluminum diaphragms were used and they were punctured with a hand operated plunger after preset charges of gas were placed in the tube. The plunger method provided repeatable shock velocities which were essential to obtain accurate data for comparison with shock tube theory. A small dump tank was used following the test section.

Driven pressure, p_1 , was measured with a 0-400 torr Wallace-Tiernan gauge and driver pressure, p_4 , was accurately and repeatably preset with a pressure transducer and digital readout system. The wave speed was determined for each shot using three pressure transducers to start and stop two Monsanto Model 401 timers which were accurate to within one microsecond. The pressure transducers were located on either side of the test section and the shock speed at the point of the Raman measurements was computed assuming linear shock speed attenuation. Error estimates showed that the computed speeds were accurate to within 2 percent.

For the Raman experiments, the tube was altered in several ways. A fourth pressure transducer was added near the diaphragm. The purpose of this transducer was to provide a trigger signal to fire the laser. Another alteration was the addition of a Raman test chamber near the end of the tube. Finally a support was attached to the end of the tube and bolted to the floor. The purpose of this stiffener was to minimize any vibration during the diaphragm rupturing. Removing this vibration eliminated any significant misalignment of the beam with the collection optics.

C. POSTSHOCK PROPERTIES

A pressure limit on p_4 of 325 psia was arrived at from safety considerations since the diaphragm plunger was hand operated. Also, to obtain reasonably high postshock densities p_1 was kept above 50 mm-Hg in the present experiments. p_4 and p_1 were adjusted accordingly to produce shock speeds from 1100-1600 m/sec. The above restrictions were not prohibitive since they provided a postshock temperature range of approximately 750-1400°K and densities from about 0.35-0.75 the density of air at STP conditions.

Another postshock parameter which had to be considered was the vibrational excitation time of a gas constituent compared to the test time of the shock tube. The excitation time had to be shorter than the test time or equilibrium conditions could not be achieved behind the wave. The test time ranged from 100-300 μ sec, therefore, only pure oxygen or O_2 in air could be investigated for lower speed shocks. At the higher shock velocities, the properties of N_2 in air were investigated. Pure N_2 could not be examined at any equilibrium conditions in the present tube because of the long excitation times compared with the test time restrictions.

IV. RAMAN INSTRUMENTATION FOR SHOCK TUBE DIAGNOSTICS

A. GENERAL DISCUSSION

The application of Raman spectroscopy to a shock tube environment is in general a straightforward process of obtaining the required scattering data at the proper time and within a short time interval. Also, the measurements must be made in a small region within the center of the tube. The recording time must be short in order that instantaneous and not time averaged results are obtained within the test time. When rate measurements are being made, the measurement time must also be short compared to the nonequilibrium thermochemical times associated with the shock heating process. The scattering volume must be small to avoid boundary layer regions of the flow which would complicate the calculation of postshock gas properties. A small scattering volume dimension parallel to the shock front is also required if accurate time histories are to be obtained behind the wave for thermochemical rate measurements.

The particular experimental instrumentation and associated optical apparatus necessary to fulfill the above requirements are discussed in the following sections.

B. OVERALL EXPERIMENTAL SETUP

A schematic of the Raman scattering apparatus for the present shock tube measurements is shown in Figure 5. Figure 6 is a photograph of the setup which emphasizes the optical components and the path of the laser beam. In Figure 7, a view of the entire experimental setup is shown which includes the spectrum analyzer and recording oscilloscope.

Since the shock tube generates high temperatures and pressures for only a few hundred microseconds and thermochemical times can be orders of magnitude less than that, pulsed lasers are best suited for Raman measurements in these transient flow facilities. Hence, a 100 megawatt pulsed ruby laser with a pulse width of 20 nanoseconds was used as the monochromatic source.

The ruby radiation at 6943 Å traveled along a path under the shock tube and in a direction parallel to the tube's axis. The beam was then rotated 90° as shown in Figure 5. Two right angle internal reflecting prisms were actually used as shown in Figure 6 to

properly turn the horizontally polarized beam and also rotate the axis of polarization so that it was in the plane of the paper as the radiation passed through the test volume. The 1 centimeter diameter beam was then focused with a cylindrical lens into the center of the 25 mm diameter tube. A 6 mm diameter spatial filter was used to obtain a 1 x 6 mm beam dimension. Intersection of this beam volume with the 0.5 x 6 mm high slit image of the spectrum analyzer defined a 0.5 x 6 x 6 mm scattering volume shown in Figure 5. Thus, the measured densities and temperatures were obtained from light scattered within the above volume. This small spatial resolution implied that good time resolution was obtained behind the shock wave and also insured that boundary layer effects were negligible. Comparison could then be made of Raman data with simple shock tube theory.

After passing through the test region, the laser radiation was collected in a light trap to avoid detection by the Raman signal processing instrumentation. A small portion of the incident radiation was first diverted with a beamsplitter to the laser power monitor which consisted of a photodiode and appropriate attenuation filters. The power monitor was required in order to record pulse-to-pulse variation in the laser output. Since the Raman signal is proportional to the incident laser intensity, this variation was ratioed out to obtain accurate Raman intensities. Note that only relative intensity measurements are required so absolute laser power measurements are not necessary. This fact will be discussed in more detail later in the report.

As shown in Figure 8, the Raman scattered light at 90° to the incident laser beam was collected with a f/2.5 lens located a focal distance of 13 mm from the scattering volume. A f/5 lens focused the collected radiation on to the slit of the spectrum analyzer.

C. ELECTRO-OPTICAL COMPONENTS

The scattered light collected by the optics must be analyzed to determine its spectral content. In the present experiment a 3/4 meter f/6.7 Spex spectrometer was used. A 600 gr/mm grating blazed at 1μ was employed in conjunction with 1 mm slit. This combination resulted in an apparatus function which was nearly triangular with a 1/2 bandwidth of 22.5Å in the first order. The true apparatus function, $A(\Delta\lambda)$, was measured with a helium neon laser and the data fit with mathematical functions. These equations were coded into the Raman theoretical intensity program to predict the unresolved spectra as a function of temperature using Eq. (13).

After the scattered light was spectrally analyzed it was converted to an electrical signal by an RCA 31034A photomultiplier tube, PMT, which was selected for a high quantum efficiency of 19 percent at 8600Å. Before reaching the PMT, the light passed through a laser blocking filter. The filter used in the present study was a 3 mm thick piece of RG-N9 black glass made by Schott Optical Glass, Inc.

This filter transmitted 85 percent of the incident radiation at wavelengths greater than 7700Å (i.e., the Raman region of interest) yet blocked ruby laser radiation by a measured factor of nearly 10^5 . The filter was used to eliminate laser radiation which was not removed by the spectrometer. Removing this unwanted light was necessary to prevent masking of the weak Raman radiation from the test gas.

Raman signal from the PMT was recorded on channel #2 of a Tektronix 454 oscilloscope using an EG&G Model IT 100 inverting transformer to invert the negative PMT signal. A 50 Ω feed-through terminator followed the inverting transformer to provide fast response times in order to accurately record the 20 nanosecond pulses. A positive output signal from the Korad KD-1 photodiode incident laser intensity monitor was also terminated in 50 Ω and recorded on the same oscilloscope by feeding this signal into channel #1 and putting the scope in the "add" mode. Since there was approximately a 100 nanosecond transit time of the electrons through the dynode channel of the PMT, then this signal arrived after the photodiode signal. Hence, both were recorded on the same instrument. An example oscilloscope trace recorded in this fashion is shown in Figure 9. A trace of this type was obtained for each laser firing. Data points then correspond to ratioing the Raman signal, I_R , to the laser signal, I_L , taken off the same trace.

The oscilloscope sweep was triggered by utilizing the negative energy pulse which is also provided by the KD-1 photodiode circuit at the time the laser is fired.

D. COINCIDENCE TIMING

As mentioned above, the laser had to be fired at the proper time behind the shock front. At first the solution to this problem seemed to be a simple matter of using a single transducer to provide an output when the shock wave passed a certain point. This output could be suitably delayed to fire the laser at the proper time. However, the nature of a ruby laser firing sequence complicated matters somewhat. The ruby rod must be optically pumped with a flash lamp for approximately 1 millisecond before a giant pulse can be obtained by Q-switching the cavity. Hence, using a single trigger meant that flash lamp triggering would occur when the shock wave was only about half way down the tube. Small variations in shock speed were amplified over a long distance and a 50 μ sec jitter was encountered in the time that the laser was fired with respect to passage of the shock front. The actual position of the wave with respect to the laser firing was easily obtained to a high degree of accuracy by using the KD-1 photodiodes' negative energy pulse to start a timer which was stopped by passage of the wave by position #3 in Figure 5. However, using a single transducer, the actual measured time would be a large random scattered value around a preset time rather than the value picked by the experimenter.

To remedy this situation, one transducer located near the diaphragm (i.e., transducer DT in Figure 10) and delay was used to fire the lamp while a second transducer and delay fired the Q-switch. This second

transducer (i.e., #1 in Figure 10) was located near the scattering volume in order to obtain a jitter of only ± 2 microseconds. Other details of the timing and coincidence circuitry are shown in Figure 10. Each trigger circuit consisted of a pressure transducer and a cathode follower amplifier which was used to drive a trigger generator. The 5 volt output of the trigger generator started a preset delay. The 15 volt output of the delay provided a trigger signal compatible with the laser circuitry. Using this two trigger method, the transducer signals were suitably delayed to obtain both maximum pumping of the laser rod for efficient lasing and proper orientation of the shock front with respect to the viewing port. The Q-switch transducer was also used to start two Monsanto counter timers for shock speed measurements as mentioned above.

V. SHOCK TUBE RAMAN DATA

A. TIME HISTORY OF SCATTERING INTENSITY

Raman scattering intensities were monitored as a function of time as a shock wave passed the viewing port. Incident laser intensities were also recorded and I_R/I_L ratios were obtained. Results of these measurements are shown in Figure 11. Each data point corresponded to a single firing of the shock tube. The laser was also fired once with each shot but with a variable delay. Hence, the first portion of the data (i.e., open circles) at $\lambda = 8280\text{\AA}$ in Figure 11 was scattering from nitrogen ahead of the wave at the initial driven gas conditions (i.e., $\rho = \rho_1$). The final data points correspond to scattering from shock heated nitrogen. At 62 μsec before the wave passes position #3 (see Figure 5), the Raman scattering intensity increases abruptly. This increase represents the passage of the wave through the scattering volume. The constant intensity conditions behind the wave lasted for approximately 150 μsec . After that time a second abrupt change in scattering intensity occurred. This second increase was most likely due to passage of the contact surface through the scattering volume. The measured test time compared quite closely to the estimated value for the experimental conditions listed in the figure.

To insure that the output in Figure 11 was not some false signal, the intensity at $\lambda = 8310\text{\AA}$ was also measured as a function of time (i.e., square symbols in Figure 11). Note that negligible output was obtained at this wavelength which was just outside the N_2 Raman region. Hence, the recorded output at 8280\AA was truly due to Raman scattering from nitrogen.

Also shown in Figure 11 (i.e., diamond symbols) is the amount of scattering obtained from 600 torr of nitrogen at static conditions. This pre-shot data was used as a calibration bench mark to determine the absolute density prior to and behind the wave. The data in Figure 11 was reduced to true density ratios by dividing each data point by the average intensity value of $I_R/I_L = .13$ ahead of wave. The data was also corrected for temperature effects as discussed in Section II-D. This temperature correction will be further clarified in the following sections. The measurements in Figure 11 were also adjusted by subtracting 62 μsec from the recorded times. The results of this entire data reduction process are shown in Figure 12. Also shown in the figure is the theoretical plot for density ratio based on constant ratio of specific heat of $\gamma = 1.4$. This theory was picked

because, for pure nitrogen under the present experimental conditions, the vibrational mode would not be excited in the short test time encountered in this experiment. Note that the measured ratio was 10 percent greater than the theoretical prediction for this particular case. This disagreement was reasonable considering that the data in Figure 12 were, to the author's knowledge, the first Raman measurements behind a shock wave and much was learned about improving the experimental procedure following this initial data gathering sequence.

B. DETERMINATION OF VIBRATIONAL EXCITATION TIME FOR OXYGEN IN AIR

As discussed in Section II-E, the vibrational excitation time for a gas can be determined by examining the Raman scattering profile as a function of time behind the wave. This time history data was obtained for oxygen vibrational excitation in air at a shock velocity of approximately 1100 meters/sec and initial air pressure of 150 torr. The data consisted of measuring the ratio of the Raman scattering intensity at $\lambda_1 = 7762\text{\AA}$ to the incident laser intensity at various times relative to the passage of the shock front. The results are shown in Figure 13. Also plotted for illustrative purposes in the figure are the constant density profile shapes for various shock conditions and the positions on the time history plot where these conditions prevail. Note that the first profile represents static gas at ambient conditions ahead of the wave. The Raman profile for this condition is symmetric indicating negligible upper level rotational or vibrational excitation. The second condition labeled (2) on the plots is indicative of the state of the gas immediately behind the shock wave. Here the rotational temperature has increased to at least the equilibrium value behind the wave while the vibrational temperature still remains at the low ambient value. The increase in rotational temperature results in a change in the profile to a more asymmetric shape as shown in the figure. The asymmetry is caused by the increased population of the upper rotational states of the oxygen molecule. Note that the increase in Raman intensity between (1) and (2) appears to be only a factor of 3 due to the profile changes alone. However, the data indicates a change closer to a factor of 12. The apparent difference between these two factors is explained by the fact that the density also increases behind the wave by a factor of 4.

Finally, the vibrational mode excitation increases with time behind the wave until the third condition is reached. This final state represents fully excited vibration and rotation which results in a further asymmetry in the Raman profile.

This final Raman intensity increase at λ_1 was approximately a factor of 2 as noted from the theory and experimental data. The time between condition (2) and (3) is defined as the vibrational excitation time for oxygen in air.

Also shown in Figure 13 is the theoretical Raman intensity ratio represented by the solid line. Note that a dashed line was used between (2) and (3) to indicate that this path is not being exactly represented.

The prediction would be quite complex for several reasons. There would actually be a rotational temperature overshoot occurring just behind the wave and the exact vibrational temperature and rotational temperature would be difficult to predict. In actuality, there is no real need to know the exact path because only the end points are required for this excitation time measurement. In Figure 13 the theory has been implicitly corrected for temperature effects by accounting for profile changes with temperature. In fact, the existence of temperature effects is the reason behind the ability to measure the vibrational excitation process.

Note that the measured Raman intensities at the end points agree quite well with the predicted values. However, the measured time of 36 μsec shown in Figure 13 is 30 percent greater than the theoretically predicted value of 27 μsec .

The theoretical excitation time was computed utilizing experimental results determined in other shock-tube experiments using interferometric techniques. First the times had to be converted to lab fixed coordinates from wave fixed values since the Raman measurement was in the lab fixed coordinate system. To convert from one system to another the following formula is used:

$$t_{\text{Lab}} = \frac{p\tau_w}{p_2(\rho_2/\rho_1)} \quad (17)$$

where t_{lab} and τ_w are the lab and wave fixed values, p_2 is the post-shock pressure and (ρ_2/ρ_1) is the density ratio across the shock. τ_w for oxygen excitation in air (i.e., $\tau_{\text{O}_2\text{-Air}}$) is given by:

$$\frac{1}{p\tau_{\text{O}_2\text{-Air}}} = \frac{\eta_{\text{O}_2}}{p\tau_{\text{O}_2\text{-O}_2}} + \frac{\eta_{\text{N}_2}}{p\tau_{\text{O}_2\text{-N}_2}} \quad (18)$$

In Eq. (18) η_i is the mole fraction of gas i in air. $p\tau_{\text{O}_2\text{-O}_2}$ and $p\tau_{\text{O}_2\text{-N}_2}$ are given by:

$$p\tau_{\text{O}_2\text{-O}_2} = 10^{56} (T^{-1/3} - .03)^{-8} \text{ [atm-sec]} \quad (19)$$

$$p\tau_{\text{O}_2\text{-N}_2} = 1.4 p\tau_{\text{O}_2\text{-O}_2} \text{ [atm-sec]} \quad (20)$$

Eq. (19) was obtained from shock tube data by White and Millikan.¹⁵
 Eq. (20) was obtained from observations of Blackman¹⁶ showing that N_2 is 40 percent as effective as O_2 in the V-T excitation of O_2 .

C. TEMPERATURE AND DENSITY DETERMINATION USING SPECTRAL SCAN METHOD

As discussed in Sections II-D and II-E, the thermochemical state of a gas can be determined by measuring its Raman scattering spectrum. This intensity versus wavelength data can then be used to obtain the temperature and density of various species in a gas mixture. In this section, the postshock temperature and density measurements of O_2 and N_2 in air are discussed.

The objective was to determine equilibrium gas properties and compare the Raman measurements to equilibrium theoretical calculations. To insure that indeed local thermodynamic equilibrium (LTE) did exist during the test time, calculations were made of the vibrational excitation times and these computed values were compared to the expected test time in this particular experiment. As discussed in Section III-D, and V-A, pure N_2 could not be examined under equilibrium conditions due to its slow excitation time. However, calculations showed that O_2 in air was sufficiently rapid such that equilibrium conditions could be obtained over a wide range of conditions. Also, N_2 in air could be examined at higher shock velocities due to the enhanced rate of the N_2 V-T process in the presence of oxygen. For LTE conditions, the temperatures of the various modes are equal to the translational temperature of the gas (i.e., $T_r = T_v = T$). As discussed at the end of Section II-C, a broad apparatus function can be employed in this case. The following data was thus obtained using the measured apparatus function with a width at half height of 22.5Å.

To obtain accurate Raman temperature and density measurements using LRS in shock tube experiments, various precautions had to be observed during the data taking sequence. The first step was to make sure that the scattering volume was properly aligned with the spectrometer slit. This was accomplished by translating the f/2.5 lens in Figure 8 in a direction perpendicular to the slit height. This adjustment traversed the narrow 1 mm beam image across the 1 mm slit width. Raman intensity at a fixed wavelength and pressure was then obtained as a function of lens position prior to a data gathering sequence. The position of peak scattering intensity was found and the lens location set at that position. The intensity versus position profile was relatively flat near the peak value. However, periodic checks showed that small adjustments were required to maintain proper alignment. The stiffener which was added to the tube helped to reduce misalignment problems.

¹⁵White, D. R. and Millikan, R. C., "Vibrational Relaxation in Air," AIAA Journal 2, pp. 1844-1846, October 1964

¹⁶Blackman, V., "Vibrational Relaxation in Oxygen and Nitrogen," J. Fluid Mech. 1, pp. 61-85, May 1956

The next step was to obtain a Raman spectral scan at static conditions for the particular gas to be measured in the postshock state. This data consisted of ratioing Raman scattering intensities to incident laser intensity values (i.e., I_R/I_L) for various wavelengths throughout the Raman region. The results of such a scan for nitrogen in air are shown on the upper plot in Figure 14. This raw data was obtained by evacuating the tube to a pressure of 200 torr of air prior to a given testing period. Each data point (i.e., open symbol) corresponds to a single laser firing but at a different indicated spectrometer wavelength position, λ_I . Note that some residual intensity not associated with Raman scattering was present outside the N_2 Raman region (i.e., $I_{BC} = .2$). This background light was probably due to photons produced from fluorescence of the liquid absorber used in the laser dump. The measured Raman intensities had to be corrected for this effect by subtracting I_{BC} from the data in Figure 14 to obtain I_C , the true calibration intensity. After this background light subtraction was accomplished, the data was normalized with the peak intensity value, I_{maxC} , using the following formula:

$$\bar{I} = \frac{(I_R/I_L) - I_{BC}}{I_{maxC}} = \frac{I_C}{I_{maxC}} \quad (21)$$

Note, the value of I_{maxC} in Eq. (21) was obtained by drawing a smooth line through the data points (i.e., in Figure 14, $I_{maxC} = 2.30 - .20 = 2.10$). The purpose of obtaining the normalized static scan may not be obvious at this time. However, to this point in the data gathering sequence, the discussion has centered around indicated spectrometer wavelength positions, λ_I . These values are not a priori equal to the actual wavelengths appearing at the exit slit of the spectrometer. In fact, it would be fortuitous if they were. A wavelength calibration procedure using standard lamp sources was helpful in determining an approximate value of the wavelength correction, Δ , given by:

$$\Delta = \lambda_I - \lambda_A \quad (22)$$

Here λ_A is the actual wavelength position while λ_I is the position that is indicated on the wavelength dial of the instrument. But, Δ is a small but non-negligible function of λ_A itself so the calibration source wavelength would have to be located almost identical to the Raman wavelength. This was not practical for the present experiment, so, instead, the Raman data from Eq. (21) at known static conditions was used to accurately determine the Δ to be used to correct the spectrometer wavelength settings. $\Delta = 20\text{\AA}$ was determined from the normalized form of the data in Figure 14. For purposes of comparing pre- and postshock data, the static Raman output in Figure 14 was further reduced to values indicative of initial preshock conditions

(i.e., $p = p_1$). This was accomplished by multiplying the intensities that were corrected for background light by a ratio of the initial pressure, p_1 , to the pressure at which the static scan data was obtained (i.e., $p = p_{\text{calib}}$). Hence:

$$I_{1M} = I_C \times \frac{p_1}{p_{\text{calib}}} \quad (23)$$

Where I_{1M} are the measured static Raman scan values referenced to the initial preshock conditions. The results of this data reduction are shown as open circles in Figure 15.

To compare this static scan data to a theory, Raman spectral intensities were computed using Eq. (13) at $T = 296^\circ\text{K}$. The 22.5Å experimentally determined apparatus function was used in these calculations. The computer output intensities, \bar{I}_R , are normalized to give a peak intensity of 1. These values were then adjusted to the preshock experimental conditions using:

$$\bar{I}_{1T} = \bar{I}_R (T = 296^\circ\text{K}) \times \frac{p_1}{p_{\text{calib}}} \times I_{\text{max}C} \quad (24)$$

The theoretical Raman profile at the initial static preshock conditions, I_{1T} , is the solid curve plotted in Figure 15. I_{1T} was plotted in this figure to illustrate that the computer calculation compared well with room temperature data and also to show that the value of Δ is reasonably accurate.

Having performed the necessary alignment and wavelength calibration, the raw shock tube data was then obtained. The procedure was the same as for the static scan data except that the passage of the shock front triggered the laser to fire at the proper time behind the wave. In the present experiment this time was taken as the value after the measured excitation time and before the useful test time. The results are shown on the lower plot in Figure 14 for shock heated nitrogen in air. The postshock scan data must again be corrected for background light by subtracting $I_{BS} = .27$ from the measured Raman to incident laser intensity ratios in Figure 14 to obtain I_S , the tube scan intensity. I_S versus wavelength data is then plotted in Figure 15 using open square symbols. The postshock measurements can now be compared to static data at preshock conditions.

To relate this scan data to actual density and thus to obtain density ratios, an accurate standard calibration is required (i.e., more accurate than the static scan data previously obtained). Such a calibration simply involves measuring the Raman scattering intensity at a known pressure (i.e., $p = p_{\text{STD}}$) at ambient temperature conditions.

Furthermore this standard intensity, I_{STD} , should be measured at a fixed wavelength location (i.e., $\lambda_A = \lambda_{STD}$).

At this point it would be appropriate to say something about the magnitude and meaning of the I_R/I_L values found in Figure 14. Note that in Figure 9, $I_R/I_L = 2.27$ was obtained. The point to be made here is that this number is completely arbitrary and the absolute ratio need not be determined as long as nothing unknowingly happens to alter the sensitivity of the intensity monitoring equipment between the shock tube tests and the standard calibration sequence. To make sure the sensitivity is not changing with time, the standard calibration test should be made periodically between sets of shock tube firings. If this relative Raman calibration output (i.e., I_{STD}) at a known ambient condition is constant with time during the shock heated tests, then the sensitivities have remained constant and the calibration intensities can then be used to obtain exact results from the arbitrary intensity values shown in Figures 14 and 15. The average calibration intensity value obtained prior to and during the shock tube data sequence is also plotted as 2.18 in Figure 14 (i.e., solid circular symbol) along with the standard deviation bars representing scatter about this value. Again this calibration must be corrected for background light intensity by subtracting I_{PC} from the average value to obtain the actual standard calibration intensity (i.e., $I_{STD} = 2.18 - .20 = 1.98$). Also note from Figure 14 that the average intensity value fits quite well with the raw scan data obtained previously. I_{STD} was then altered to reflect preshock conditions so it could be used to determine the density ratio across the shock. Hence, the standard intensity at state ① conditions was given by:

$$I_{1STD} = I_{STD} \times \frac{P_1}{P_{STD}} \quad (25)$$

(i.e., $I_{1STD} = 1.98 \times 1/4 = .495$ from Figure 14)

where: $P_{STD} = P_{calib} = 200$ torr

Note that Eq. (25) represents the same correction procedure that was performed on the scan data with Eq. (23). $I_{1STD} = .495$ is then plotted in Figure 15 for comparison to the static scan data and also to reduced values of postshock data. The standard wavelength, λ_{STD} , was 8282Å.

The postshock Raman output in Figure 14 was then curve fit in order to obtain the temperature and density of nitrogen in the shock heated air. The trial curve fits produced residual error sums whose magnitude is based on how well the theory agreed with measured data. Two

variables were adjusted to obtain a minimum residual value. These variables were gas temperature and maximum intensity, I_{MAXS} , of the theoretical profile. I_{MAXS} was used to normalize the scan data to 1 in order to compare the measured values to the Raman theory which was also normalized to 1. Hence, Raman theory refers to results of Eq. (13) normalized to the peak intensity value. The curve fit results give postshock temperature, hence the temperature ratio, directly. However, to obtain the shock density ratio, further data reduction is required using the I_{MAXS} value obtained from the curve fit process. This further data reduction is straightforward and consists of finding the best fit value for the postshock intensity at $\lambda_{STD} = 8282\text{\AA}$. To accomplish this the normalized theoretical Raman spectral profile which best fit the Raman data was multiplied by I_{MAXS} to obtain I_T , where:

$$I_T = \bar{I}_R (T = T_{BEST\ FIT}) \times I_{MAXC} \quad (26)$$

Results of the calculations using Eq. (26) are then plotted for comparison with the postshock data in Figure 15. Also, the value of I_T at 8282\AA was found to be 1.89 and is labeled in the figure.

At long last, the density ratio can be computed, without correcting for temperature effects, by ratioing the two intensity values at λ_{STD} in Figure 15. Hence:

$$\left(\frac{\rho_2}{\rho_1}\right)_{\text{uncorrected}} = \frac{I_T(\lambda=\lambda_{STD})}{I_{1STD}} \quad (27)$$

(i.e., $\rho_2/\rho_1 = 1.89/.495 = 3.82$ from data in the figure)

Finally, the true density ratio can be determined from the reduced data by correcting the above for temperature effects. The reason that the temperature was not accounted for in the previous procedures is that the theoretical computations used above were always normalized to a peak intensity of 1 for convenience sake in performing the curve fit process. However, as Figure 3 depicts, the peak intensity (and hence all other intensity values) varies as a function of temperature at constant density. Hence, this temperature effect must be accounted for in the data reduction process. This was accomplished by multiplying the uncorrected value by a ratio of the theoretical Raman output at $\lambda = \lambda_{STD} = 8282\text{\AA}$ for room temperature (i.e., calibration temperature) conditions to the theoretical output at the postshock temperature. Hence:

$$\frac{\rho_2}{\rho_1} = \left(\frac{\rho_2}{\rho_1}\right)_{\text{uncorrected}} \times \frac{I_R(T=T_{ROOM})}{I_R(T=T_{BEST\ FIT})} \quad (28)$$

The theoretical Raman intensity as a function of temperature, $I_R(\lambda) = N\lambda_p$ in Eq. (13), is plotted in Figure 16 for $\lambda = \lambda_p = 8282\text{\AA}$. From the figure, at $T = T_{\text{BEST FIT}}$, $I_R = .743$ and at $T = 296^\circ\text{K}$, $I_R = 1$. Using Eq. (28), the temperature correction follows directly (i.e., $\rho_1/\rho_2 = 3.82 \times 1/.743 = 5.14$). This value is 26 percent higher than the uncorrected density ratio which indicates the importance of the temperature correction process.

The above data reduction procedure seems laborious and complex. Its description could have been simplified somewhat but a lot of the details and some of the physical meaning of the data would have been lost. Basically, Figure 14 represents the raw data containing arbitrary but consistent output sensitivities between calibration and test conditions. The raw data was corrected for background light and then referred to the initial conditions prior to the shock wave (i.e., $p = p_1$). In Figure 15, the pre- and postshock arbitrary intensity data were compared on a single plot. Temperature was obtained by a simple curve fit of the arbitrary intensity values. The density determination was more involved. Accurate pre- and postshock intensities at $\lambda = \lambda_{\text{STD}}$ were ratioed to obtain the uncorrected density ratio. This ratioing of arbitrary intensities results in a real density ratio and hence actual postshock density simply because the preshock arbitrary intensity corresponded to a known density value. The necessary factors for correcting the density ratio for temperature effects were obtained from Figure 16.

D. TEMPERATURE AND DENSITY MEASUREMENT USING 2-COLOR TECHNIQUE

In many ways, the 2-color (i.e., 2-wavelength) technique is similar to the spectral scan method in that the 2-color data essentially consists of only a three point wavelength scan. Two intensity values are obtained within the Raman spectral region and a third point at a wavelength outside the Raman band in order to determine background light intensity. The idea was to obtain more accurate data at the fewer number of points by measuring Raman and background intensities at each wavelength for three to five shock tube-laser firings. The rationale behind a 2-color technique is that the spectrometer could be replaced with a series of filters and photo-detectors. This would improve the signal gathering capabilities of the optics since filter systems can have a very low f/no. And, using three filters, all the necessary experimental data to determine density and temperature could be obtained with a single laser firing.

The same precautions regarding alignment of the scattering volume with the spectrometer slit were required for the 2-color data gathering sequence. Also, a Raman spectral scan at static conditions was again necessary to convert spectrometer wavelengths to true wavelength values. The results of this scan are shown in the upper portion of Figure 17. Note that the peak intensity value of 2.51 is somewhat different than in Figure 14 indicating a small change in the sensitivity of the system in the time between the two types of data gathering sequences. The results of Figure 17 were corrected for

background light intensity and normalized using Eq. (21), where $I_{MAXC} = 2.51 - .20 = 2.31$. The value of Δ determined from this static scan procedure was 20\AA , which was identical to the previous wavelength correction factor.

As before, I_{1M} was obtained using Eq. (23) and the results of this data reduction procedure are shown as open circles in Figure 18. Also plotted as the solid line through this data is the computed intensity profile at the calibration temperature and pressure conditions using Eq. (24).

The standard calibration results taken prior to and during the 2-color data sequence are also shown in Figure 17 with a solid circular symbol. Using Eq. (25), the standard intensity was referred to postshock conditions (i.e., $I_{1STD} = (2.28 - .20) \times 1/4 = .520$). I_{1STD} is also plotted in Figure 18 again using a solid circular symbol.

The shock tube 2-color data was then obtained and the three intensity values are shown plotted as $I_1 = 1.98$, $I_2 = 1.33$ and $I_B = .43$ with square symbols in the lower portion of Figure 17. The standard deviation of the data at these wavelength values is also shown in the figure using error bars. The smooth curve drawn through the postshock data points in Figure 17 is the expected Raman output and is presented for illustrative purposes only since no curve fitting is required for the 2-color technique. As the profile depicts, λ_1 was picked near the peak of the Raman profile while λ_2 was located in the blue shifted region of the Raman spectrum. The choice of these wavelength positions is not completely arbitrary. They were picked so that the intensity at λ_1 would be somewhat insensitive to temperature effects (i.e., $I_R(\lambda_1) \approx \text{const.} \times \text{density}$). Further, λ_2 was chosen so that the ratio $I_R(\lambda_2)/I_R(\lambda_1)$ would be most sensitive to temperature changes.

From this point, the data reduction method departs rather markedly from that of the spectral scan technique. The measured postshock Raman intensities are again corrected for background light by subtracting I_B from I_1 and I_2 to obtain:

$$I_R(\lambda_1) = I_1 - I_B = 1.55 \quad (29)$$

$$I_R(\lambda_2) = I_2 - I_B = .90$$

The postshock 2-color intensity values in Eq. (29) are plotted in Figure 18 as solid square symbols. These two values (i.e., 2-color intensities) in conjunction with $I_{1STD} = .523$ are all the reduced data needed to compute temperature and density using the 2-color method. Note, that for convenience, $\lambda_1 = \lambda_{STD}$. The solid curve drawn through the postshock data in Figure 18 represents the theoretical Raman

profile for the measured postshock temperature conditions and, again, it is only shown for illustrative purposes.

To obtain temperature from the above 2-color data, the values in Eq. (29) are ratioed to give:

$$\frac{I_R(\lambda_2)}{I_R(\lambda_1)} = \frac{.9}{1.55} = .58 \quad (30)$$

In Figure 19, the theoretical value of this ratio is computed for the particular wavelengths used in the present study (i.e., $\lambda_1 = 8285\text{\AA}$, $\lambda_2 = 8260\text{\AA}$). Finding the value of the measured ratio of .58 from Eq. (30) on the vertical axis of Figure 19 and moving horizontally until the I8260/I8285 curve is intersected, one determines directly that the measured temperature is 1440°K.

Further, the uncorrected density ratio is given by an equation similar to Eq. (27) as:

$$\left(\frac{\rho_2}{\rho_1}\right)_{\text{uncorrected}} = \frac{I(\lambda_1)}{I_{1\text{STD}}} \quad (31)$$

(i.e., $\rho_2/\rho_1 = 1.55/.52 = 3.98$ from data in Figure 18)

Again, the true density can be determined by correcting for temperature effects. This was accomplished by multiplying the uncorrected value by a ratio of the theoretical Raman output at $\lambda_1 = \lambda_{\text{STD}} = 8285\text{\AA}$ for standard ambient temperature conditions to the theoretical output at the measured postshock temperature. Hence:

$$\frac{\rho_2}{\rho_1} = \left(\frac{\rho_2}{\rho_1}\right)_{\text{uncorrected}} \times \frac{I_R(T=T_{\text{ROOM}})}{I_R(T=T_{\text{MEASURED}})} \quad (32)$$

This process is analogous to that of Eq. (28). The theoretical Raman intensity as a function of temperature at $\lambda_2 = 8285\text{\AA}$ is also plotted in Figure 19. From the figure, at $T=T_{\text{MEASURED}}$, $I_R = .615$ and at $T = 295^\circ\text{K}$, $I_R = .913$. Using Eq. (32), the temperature correction follows directly (i.e., $\rho_2/\rho_1 = 2.98 \times .913/.615 = 4.42$)

VI. DISCUSSION OF RESULTS

Excitation of pure O_2 and N_2 , as well as N_2 and O_2 in air have been discussed in this report. To clarify statements made concerning these rates, excitation times for various possible V-T processes were obtained from References 15 and 16 and plotted in Figure 20 as a function of postshock temperature. These theoretical rates are really smooth curves through data measured in shock tubes with an interferometric technique.

Pure N_2 has the slowest rate, as discussed above, and it is obvious from this figure why it could not be examined in the present experiment. Also, the plot shows that the enhanced rate of N_2 excitation in air is still quite slow except at higher temperatures. However, the O_2 in air and pure O_2 results demonstrate why O_2 excitation could be examined over a larger range of conditions.

From the time history data in Figure 13, the vibrational excitation time of oxygen in air was determined at $T_2 = 827^\circ K$. The result was referred back to wave fixed coordinates to obtain $(\tau_{O_2-Air})_{meas.} =$

$339 \mu\text{sec-atm} \pm 11 \text{ percent}$. A theoretic value at this temperature was computed to be $250 \mu\text{sec}$ using Eqs. (18)-(20). The Raman result is plotted in Figure 20 for comparison to the theoretical value for O_2 excitation in air. The 22 percent variation in measured excitation time is an estimate based on the unknown conditions between data points in Figure 13 and the shot to shot variation in the shock speed. These shock speed variations resulted in postshock temperature and excitation time changes behind the wave.

The measured excitation time was 30 percent slower than expected. This is not an unusual variation for shock tube rate data, and more measurements at various conditions should be obtained before any firm comments on accuracy can be made. However, in defense of the Raman data, the interferometric measurements for O_2 in air are restricted to temperatures above $1500^\circ K$. The present result is at a temperature about half that value so the disagreement may be real. Finally, no special care was taken to assure that the air used in this experiment was really dry. Bottled dry air was used, but the moisture content was never checked. Blackman's data showed that the presence of water vapor did result in a slight increase in the excitation time as was measured in this experiment.

To improve the present excitation time measurement, the ruby laser might possibly be used in its "normal" mode instead of the "Q-switched" condition. The former provides a longer pulse (i.e., 200-300 μ sec half width). Of course, the peak power falls off accordingly and one would pay the penalty of a loss in Raman scattering intensity within a given time period. However, total laser outputs of 10-20 joules are possible instead of 1-2 joules using the "Q-switch" mode. This increased energy implies that the Raman scattering output voltage on the oscilloscope need not decrease in proportion to the width of the laser pulse especially if a suitable RC time constant was used. Some further experiments would prove useful in determining if the "normal" mode could be applied successfully. The biggest advantage to "normal" mode operation would be that all the necessary data to make an excitation time measurement would be available from a single laser-shock tube firing. This can be contrasted to the 17 laser and shock tube shots necessary to obtain a single excitation time using the data in Figure 13.

The temperature and density ratio measurements obtained from the Raman technique for O_2 and N_2 in air at different shock speeds are shown in Figures 21 and 22, respectively. The range of postshock conditions represented by the data in the figures resulted in a temperature variation from 750 to 1400°K (i.e., $T_1 = 300^\circ K$). Absolute density variation cannot be extracted from Figure 22 directly, since variations in p_1 and shock speed occurred. The actual postshock densities ranged from .35- 75 times the density of air at ambient temperature and pressure conditions.

Note that both curve fit and 2-color results, as described in the previous section, are presented in Figure 21 and 22. The vertical bars in the figures represent the maximum and minimum ratio for each data point and they indicate the extremes that could be computed due to the Raman intensity data scattered one standard deviation about the mean intensity values. The results show that the two methods of computing temperature ratios are in good agreement with each other and with the shock tube theory also plotted in the figures. The standard error is within 12 percent for temperature and 20 percent for density measurements. This disagreement between Raman data and shock tube theory is random and is mostly attributable to the uncertainty in the measured intensities. The uncertainty is mainly due to the statistical nature of the photo-electric effect in the photomultiplier tube rather than shot to shot variation in shock speed. A greater quantity of intensity data would have improved the statistical mean and thereby increased the accuracy and reduced the standard deviation scatter. Another factor that increased the scatter at the lower temperatures was the decreased sensitivity of the spectra to a temperature change. This is shown clearly when one examines the slope of the $I_R(8260)/I_R(8285)$ ratio in Figure 19 at low temperatures.

Besides these factors, several other experimental effects, which were briefly mentioned in the text, should be reemphasized here in the discussion of the disagreement between experiment and theory.

An accurate knowledge of the actual spectrometer wavelength position during a specific Raman intensity measurement was important. The temperature and density data reduction procedure depended upon accurate λ_A values. Since the spectrometer wavelength was changed frequently between λ_{STD} and $\lambda_1, \lambda_2, \lambda_S$, etc. during a given data gathering sequence, errors could have resulted from improper knowledge of the true wavelength. Of course, the instrument's indicated wavelength was always set by turning the adjustment knob in the same direction to avoid gear backlash problems as one approached λ_1 . However, hindsight indicates that a better procedure might have been to move the wavelength setting to a value about 100Å away from the desired wavelength each time it was changed. This procedure may have produced more consistently accurate Δ values and λ_A settings. The wavelength inaccuracy problem may be an explanation for the larger density measurement error compared to temperature error. In the density ratio data reduction process, not only was the basic intensity data itself affected by wavelength errors, but the temperature correction factor was also highly wavelength dependent (see Figures 17 and 19). Further, since an accurate density is governed by a knowledge of the correct temperature, temperature errors compounded the density measurement problem.

Another problem was the change in sensitivity of the electro-optical system with time due to instrumentation drift and/or optical misalignment. The magnitude of this effect could be observed, somewhat, by looking at the change in the standard intensity value with time. However, it was difficult to adjust the data properly to account for sensitivity changes when purely statistical changes may have masked them. By obtaining all the data as quickly as possible, and allowing the instrumentation a sufficient warm-up time, the sensitivity drift effect was minimized but not eliminated.

The above factors probably were the largest error sources. They were much larger than the variation in shock speed from shot to shot which was no greater than 2 percent. Hence, theoretical postshock temperature and density ratios based on such shock speed variation were also less than 2 percent.

VII. CONCLUSIONS

A comparison between the present Raman excitation measurement and data obtained from interferometric techniques demonstrates that LRS can be a valuable tool for determining shock tube excitation rates. The inherent ability of the technique to measure properties of individual gases in a general gas mixture gives it an added advantage over other shock tube diagnostic techniques, especially in the study of homonuclear molecules. Also, various molecular modes of vibrational motion in a poly-atomic molecule are Raman active and not infrared active. Perhaps some cases even exist where certain molecular modes could only be examined using the Raman scattering method. In addition to V-T excitation times, chemical reaction times, shock structure, and other shock related phenomena could be examined.

The good agreement between Raman temperature and density measurements and known values obtained from shock tube theory for a range of postshock conditions indicates several things. The LRS technique can independently determine the density and temperature of both O_2 and N_2 in air at elevated temperature conditions to within an acceptable accuracy. Further, this high temperature calibration experiment in conjunction with low temperature studies in air and other gases implies that utilization of the Raman scattering method should greatly enhance the amount of information which can be obtained in general 3-dimensional flow fields. The method could be applied to analysis of the flow around re-entry vehicles, in rocket exhaust, and engine plumes. In addition, LRS could be used as a diagnostic technique in laser cavities, combustors, MHD channels and wherever else one desires detailed spatial information about the thermochemical state of a flowing gas.

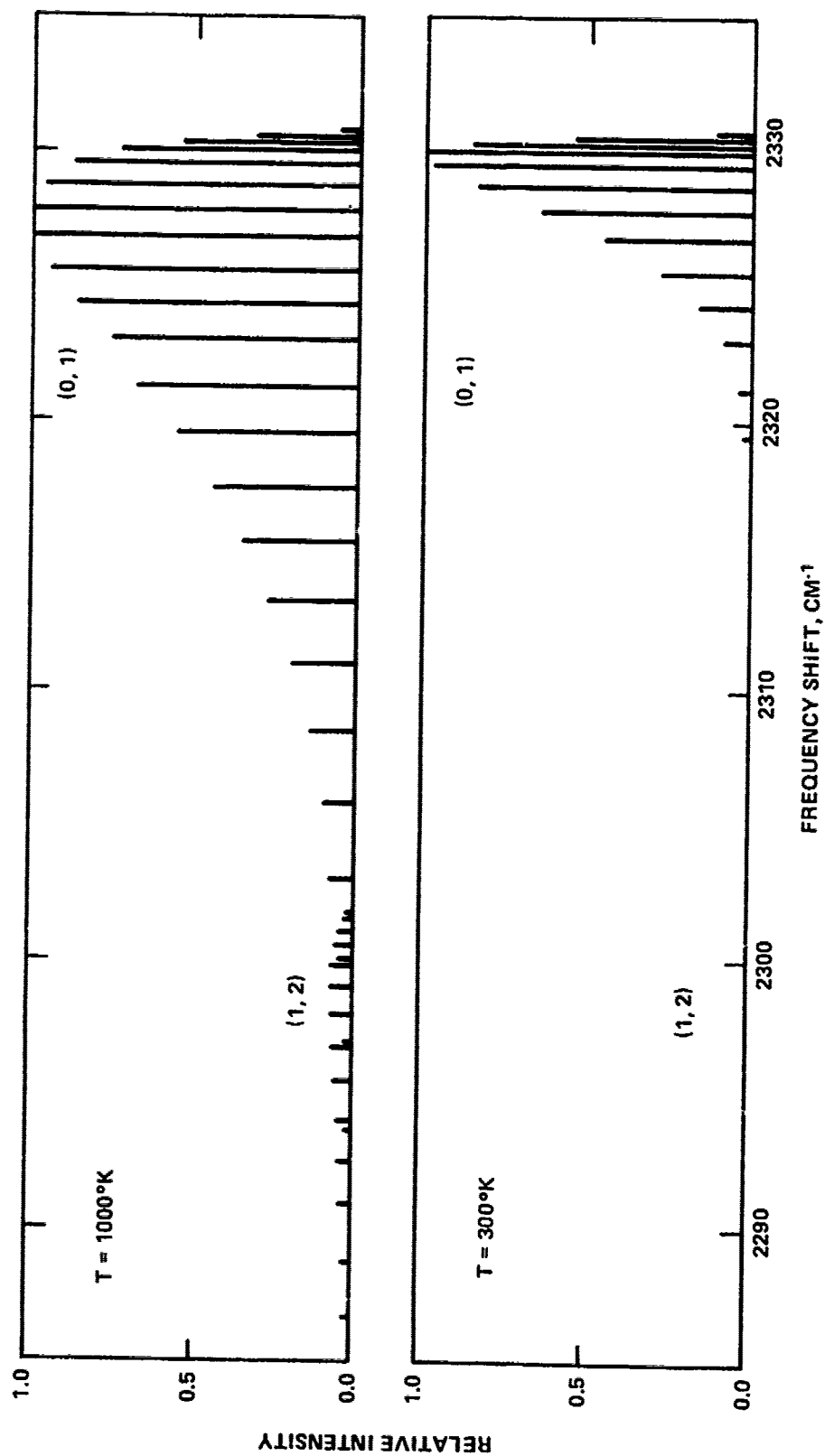


FIG. 1 CALCULATED ROTATION-VIBRATION EVEN J, Q-BRANCH LINE INTENSITIES AND FREQUENCY SHIFTS FOR MOLECULAR NITROGEN AT 300°K AND 1000°K .

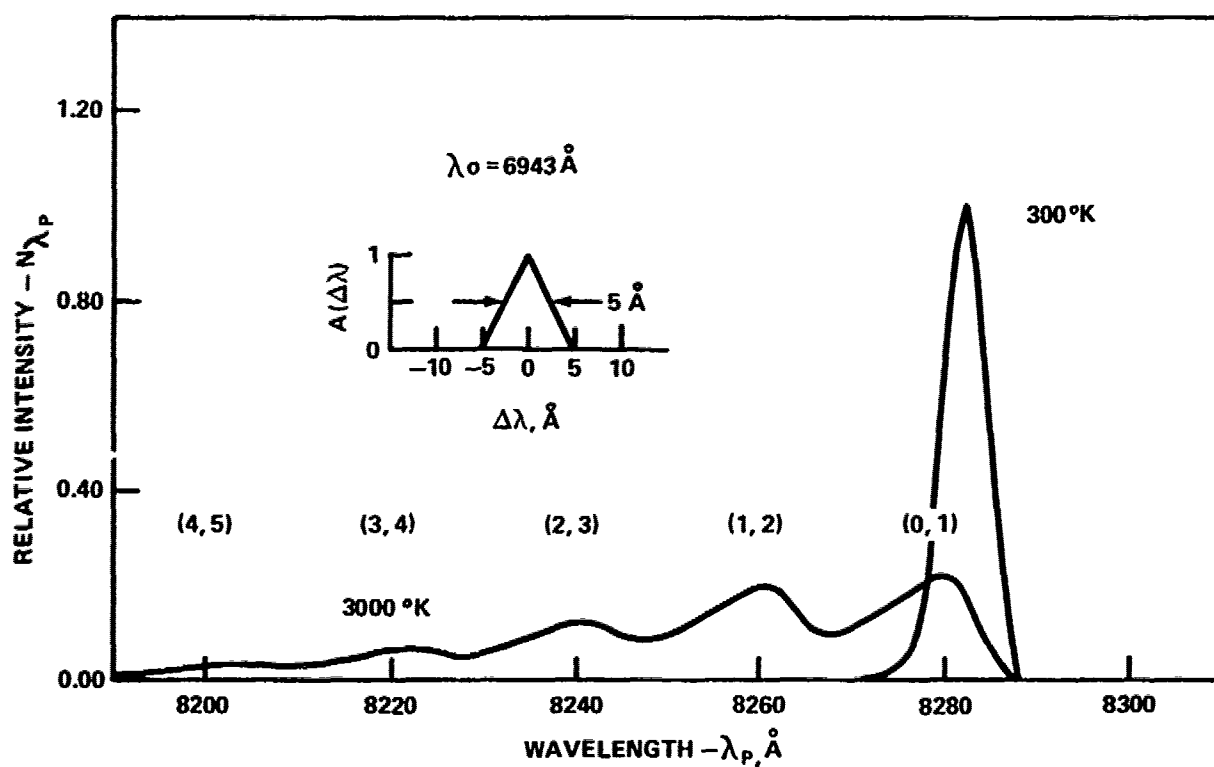


FIG. 2 UNRESOLVED STOKES ROTATION-VIBRATION SPECTRA OF NITROGEN AT $T_V=T_R=300^\circ\text{K}$ AND 3000°K COMPUTED FOR A NARROW TRIANGULAR APPARATUS FUNCTION.

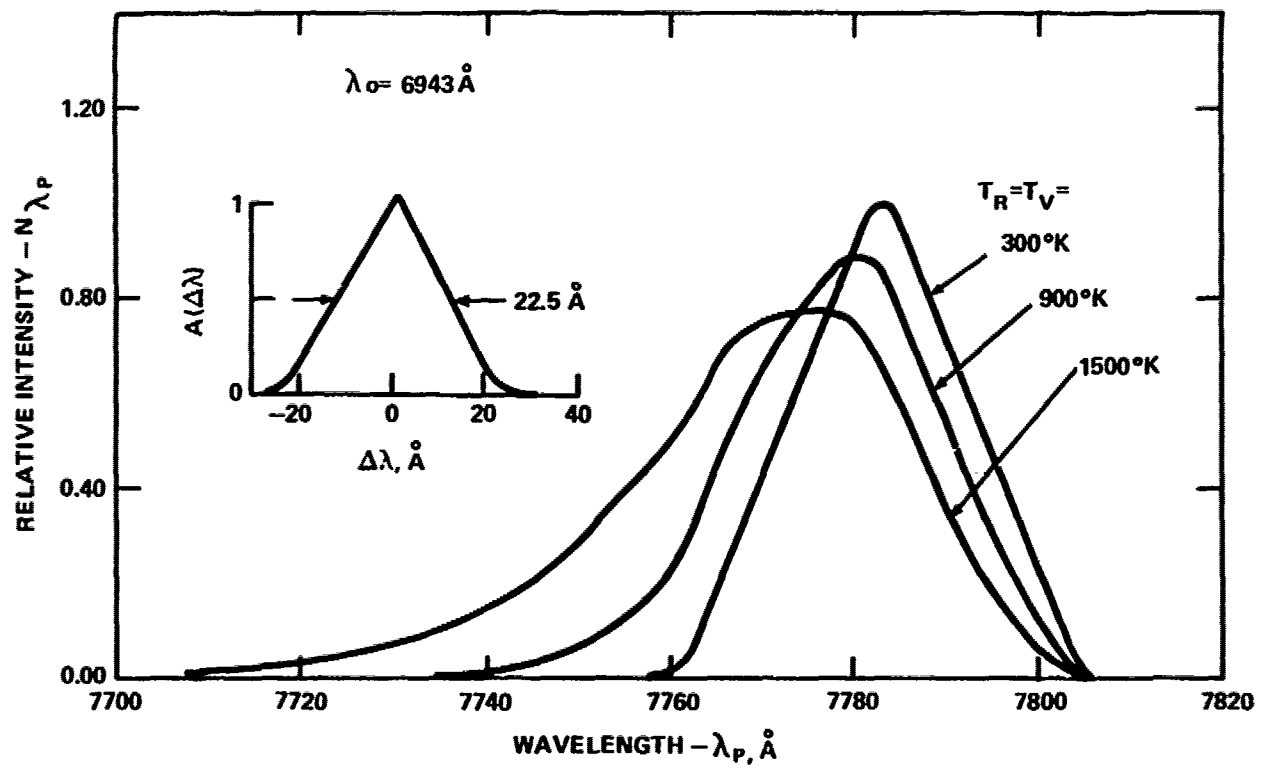


FIG. 3 UNRESOLVED STOKES ROTATION-VIBRATION SPECTRA OF OXYGEN AT $T_V = T_R = 300^\circ K$, $900^\circ K$, AND $1500^\circ K$ COMPUTED FOR THE BROAD EXPERIMENTAL APPARATUS FUNCTION.

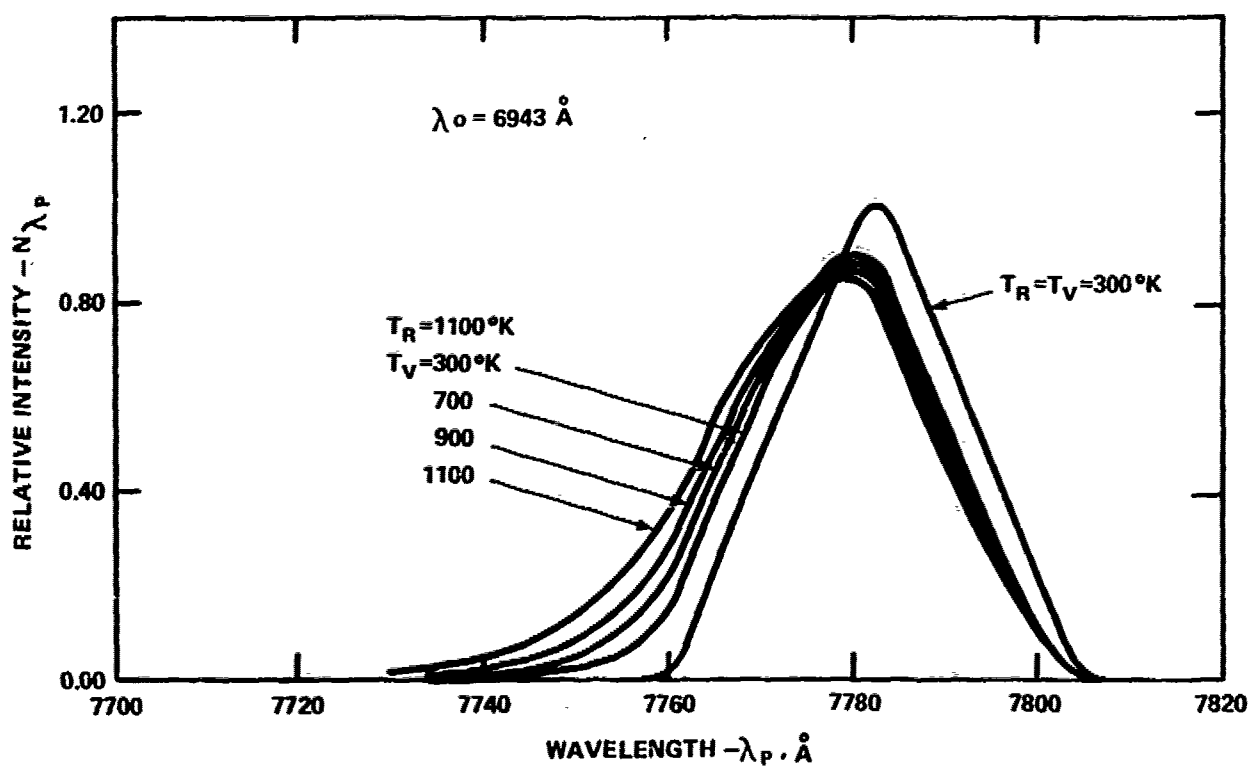


FIG. 4 UNRESOLVED STOKES ROTATION VIBRATION SPECTRA OF OXYGEN FOR NONEQUILIBRIUM CONDITIONS BEHIND AN INCIDENT SHOCK WAVE FOR $T_V \leq T_R = 1100^\circ\text{K}$.

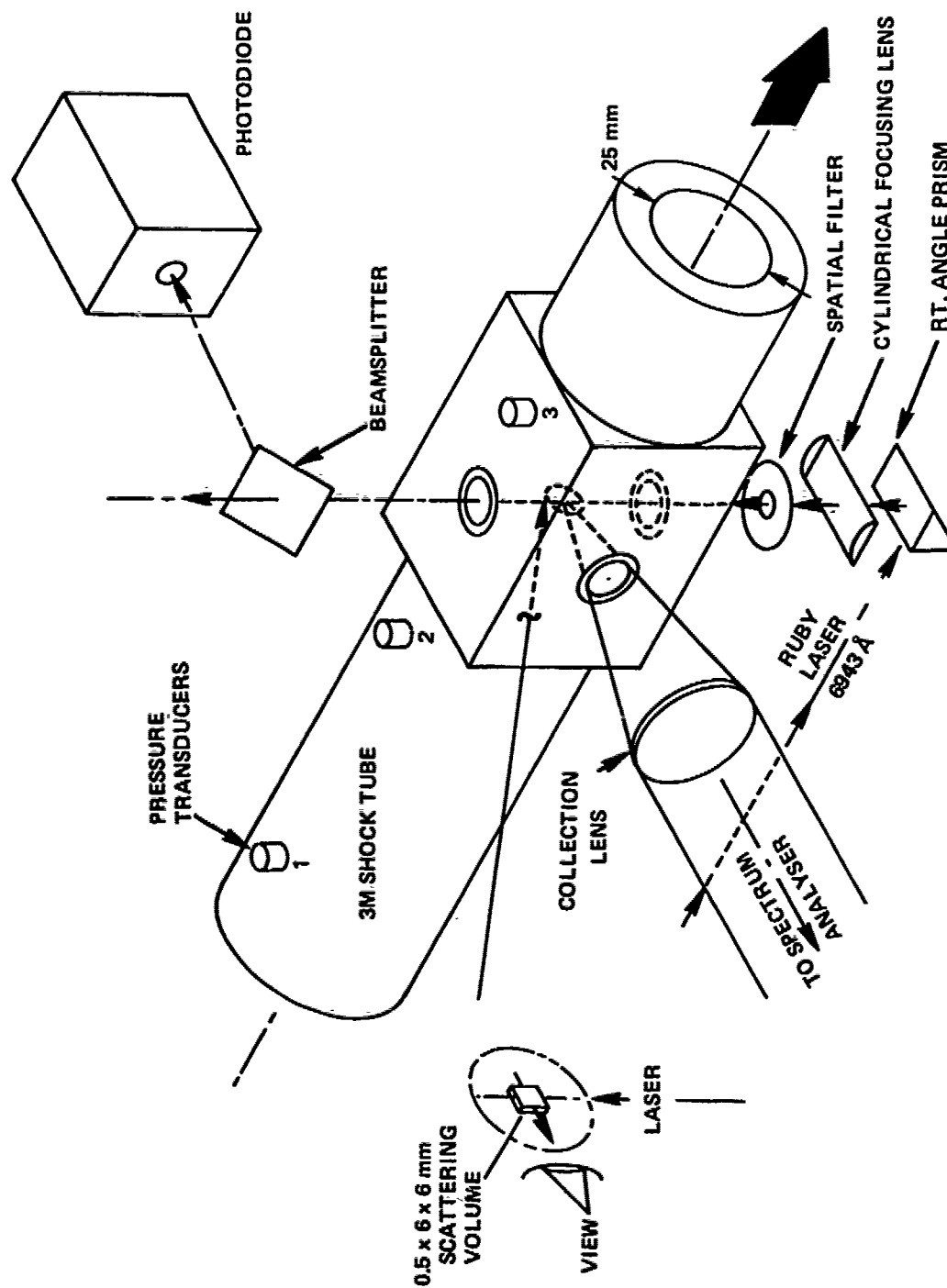


FIG. 5 SCHEMATIC OF RAMAN SCATTERING APPARATUS FOR SHOCK-TUBE EXPERIMENT

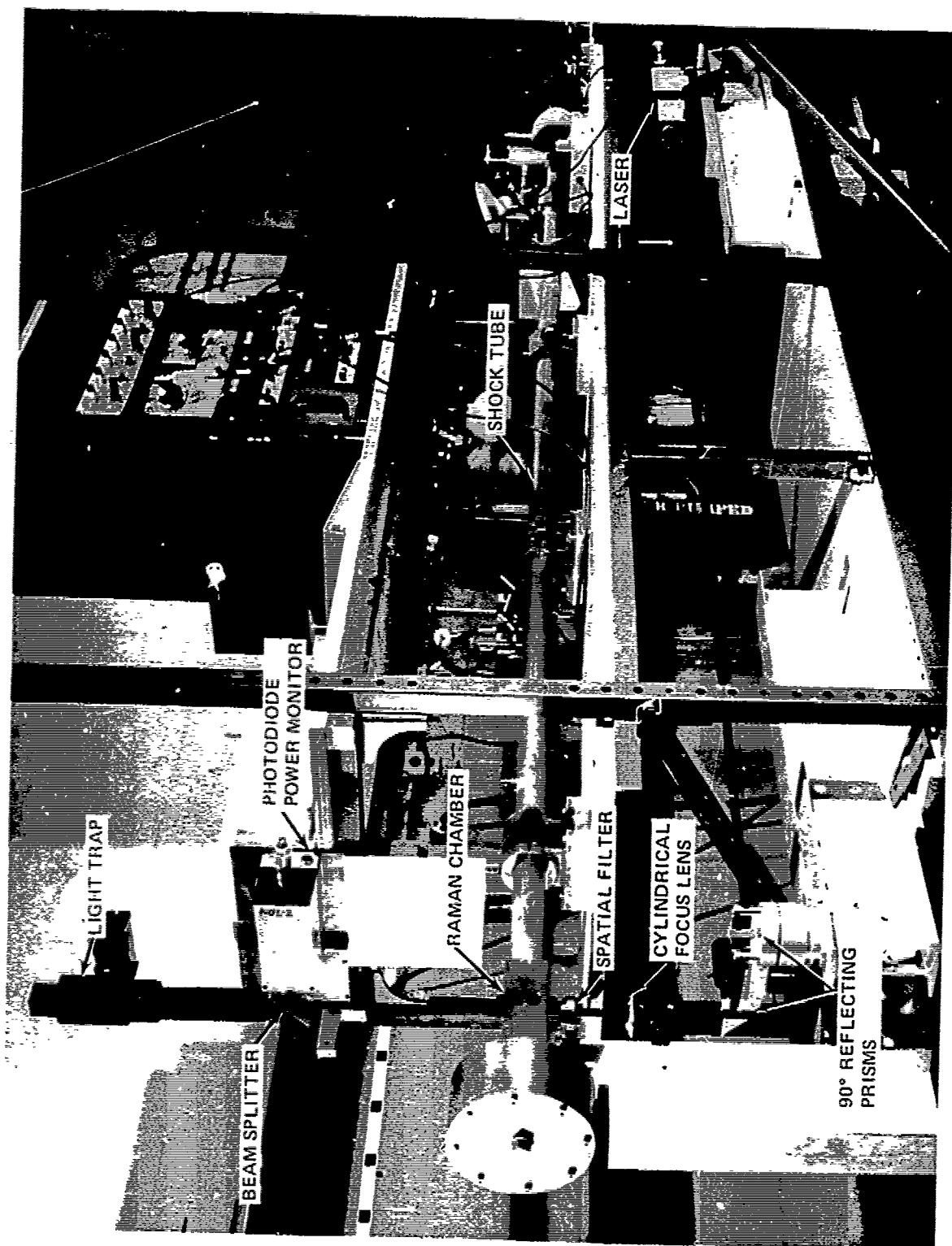


FIG. 6 RAMAN SETUP FOR SHOCK-TUBE EXPERIMENT EMPHASIZING LASER BEAM PATH

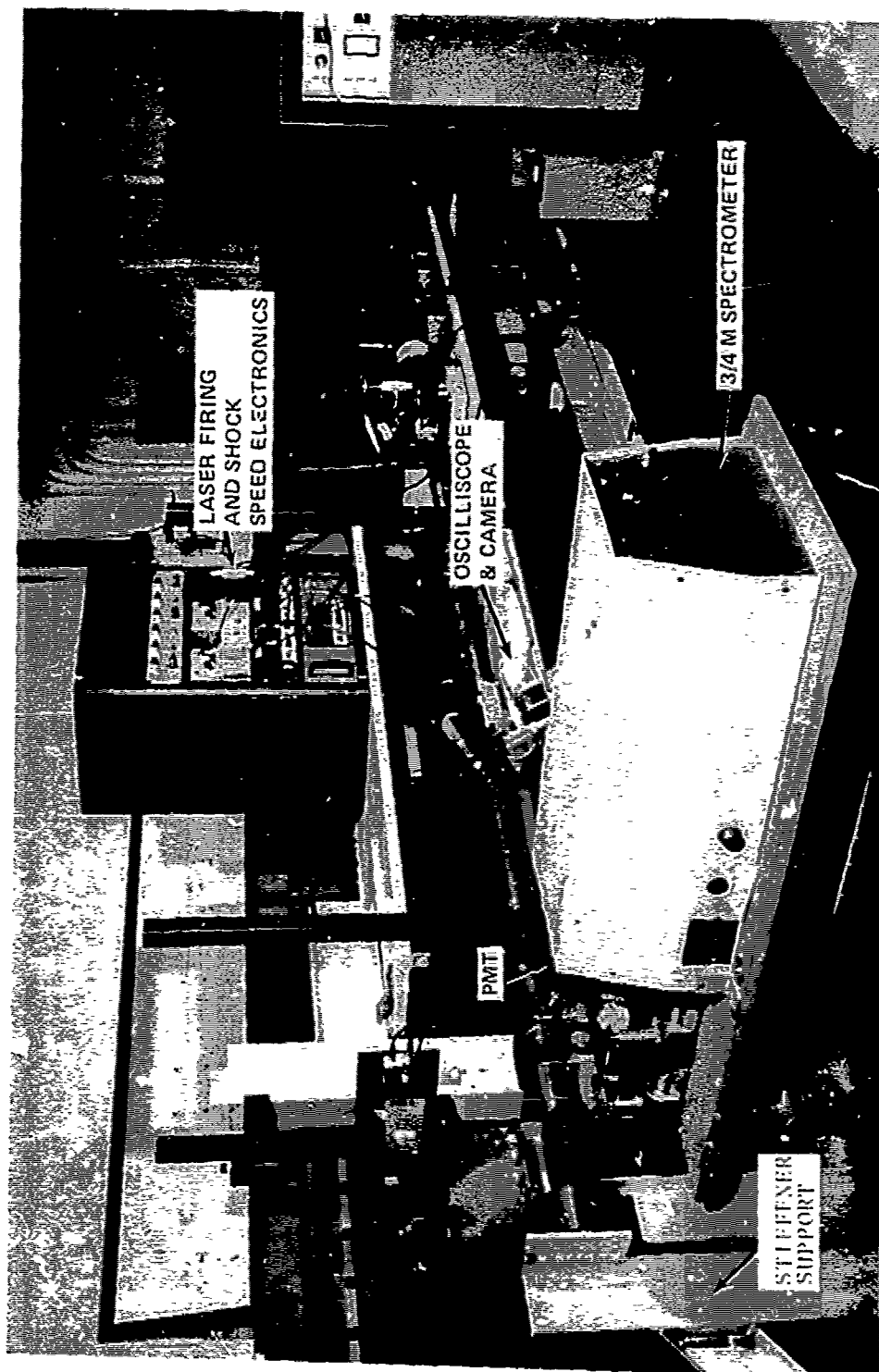


FIG.7 ENTIRE RAMAN SETUP FOR SHOCK-TUBE EXPERIMENT

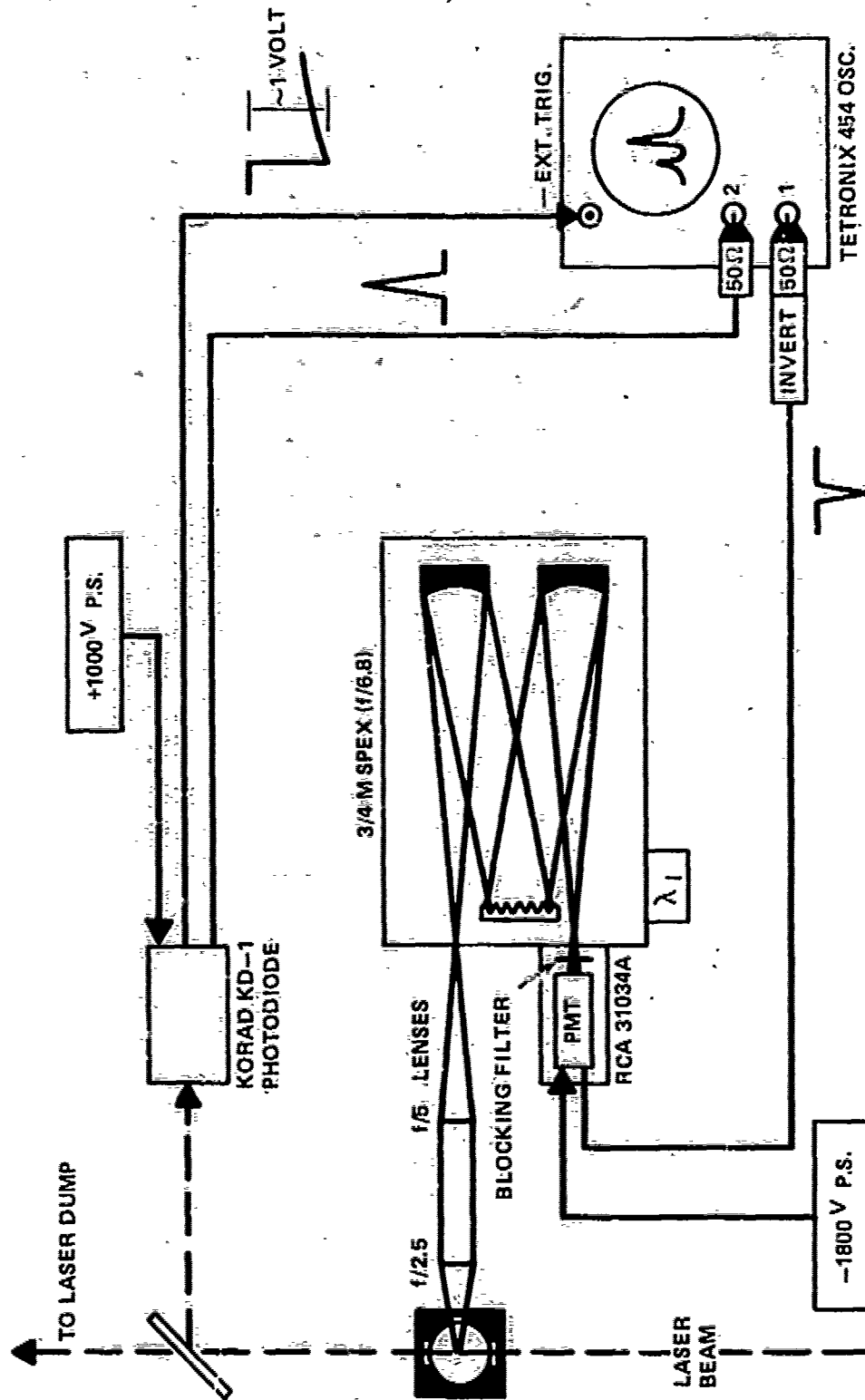


FIG. 8 SCHEMATIC OF ELECTRO-OPTICAL COMPONENTS OF DATA GATHERING SYSTEM

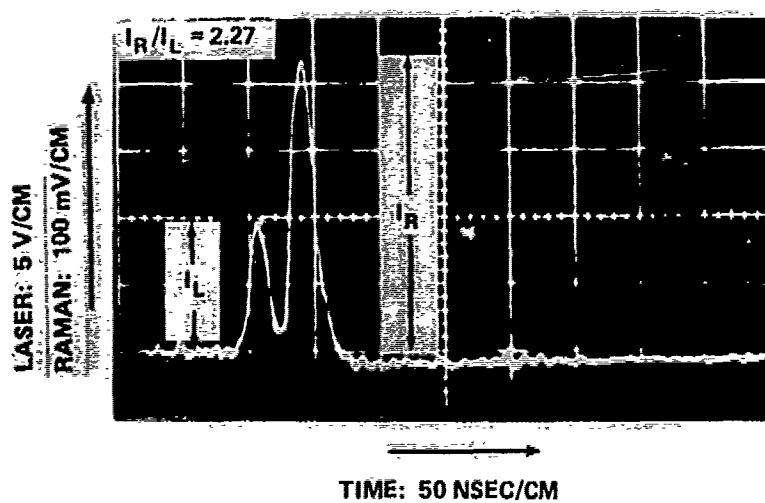


FIG. 9 OSCILLOSCOPE TRACE OF RAMAN AND LASER
OUTPUT (N_2 IN AIR - $P_{AIR} = 200$ TORR, $\lambda_A = 8283\text{\AA}$)

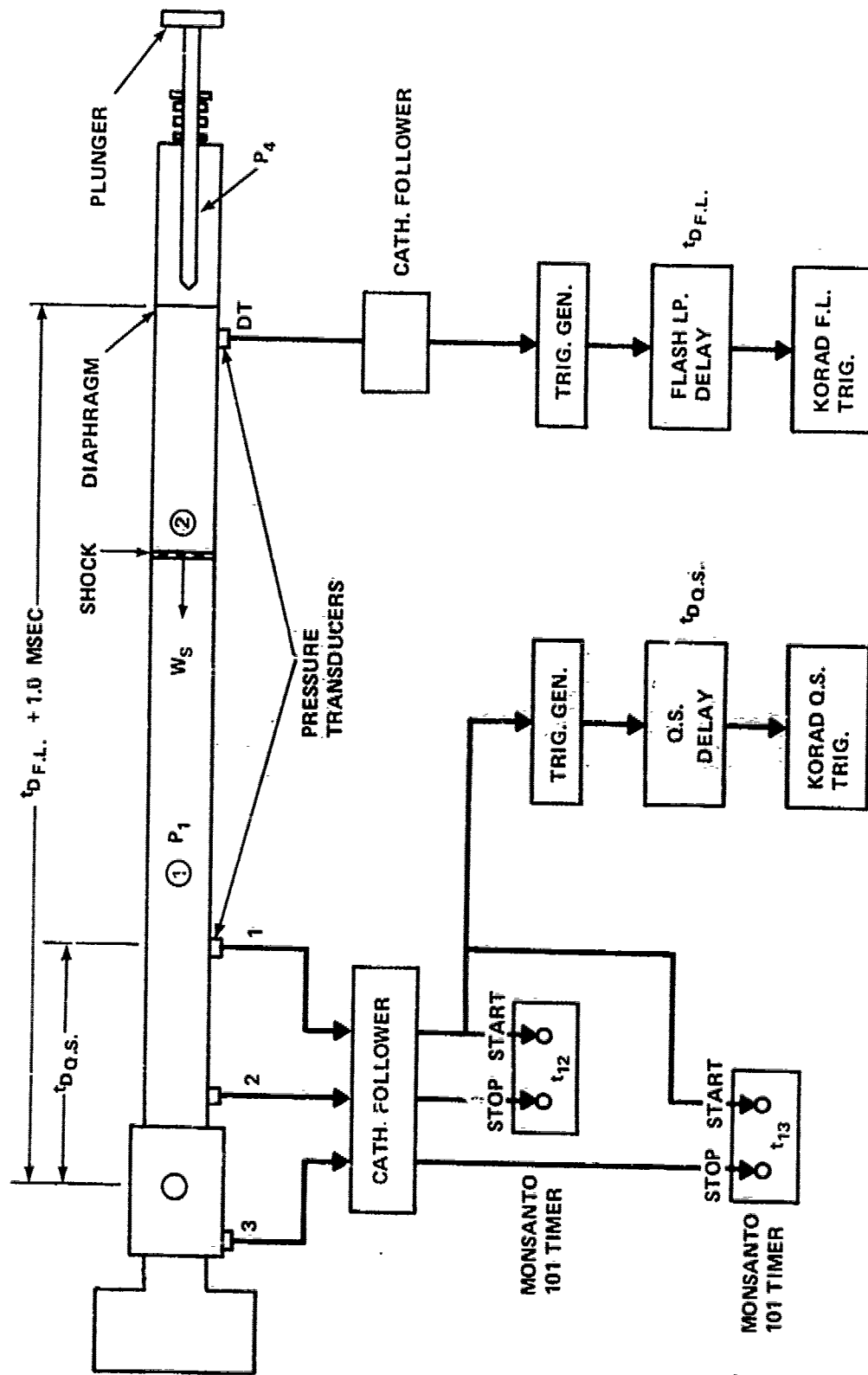


FIG. 10 TIMING CIRCUITRY FOR RAMAN SHOCK-TUBE EXPERIMENT

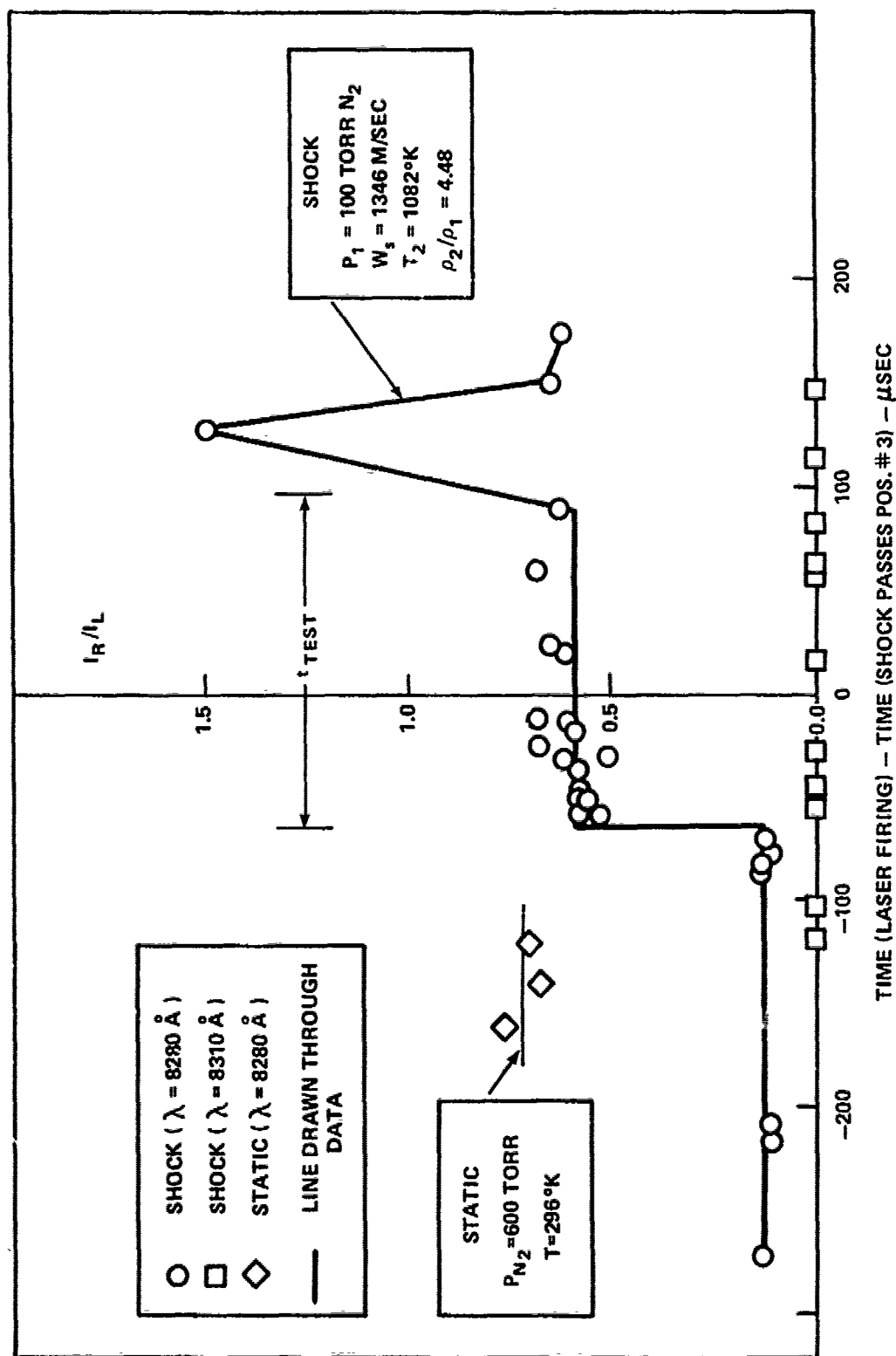


FIG. 11 TIME HISTORY OF RAMAN SCATTERING IN A SHOCK-TUBE EXPERIMENT

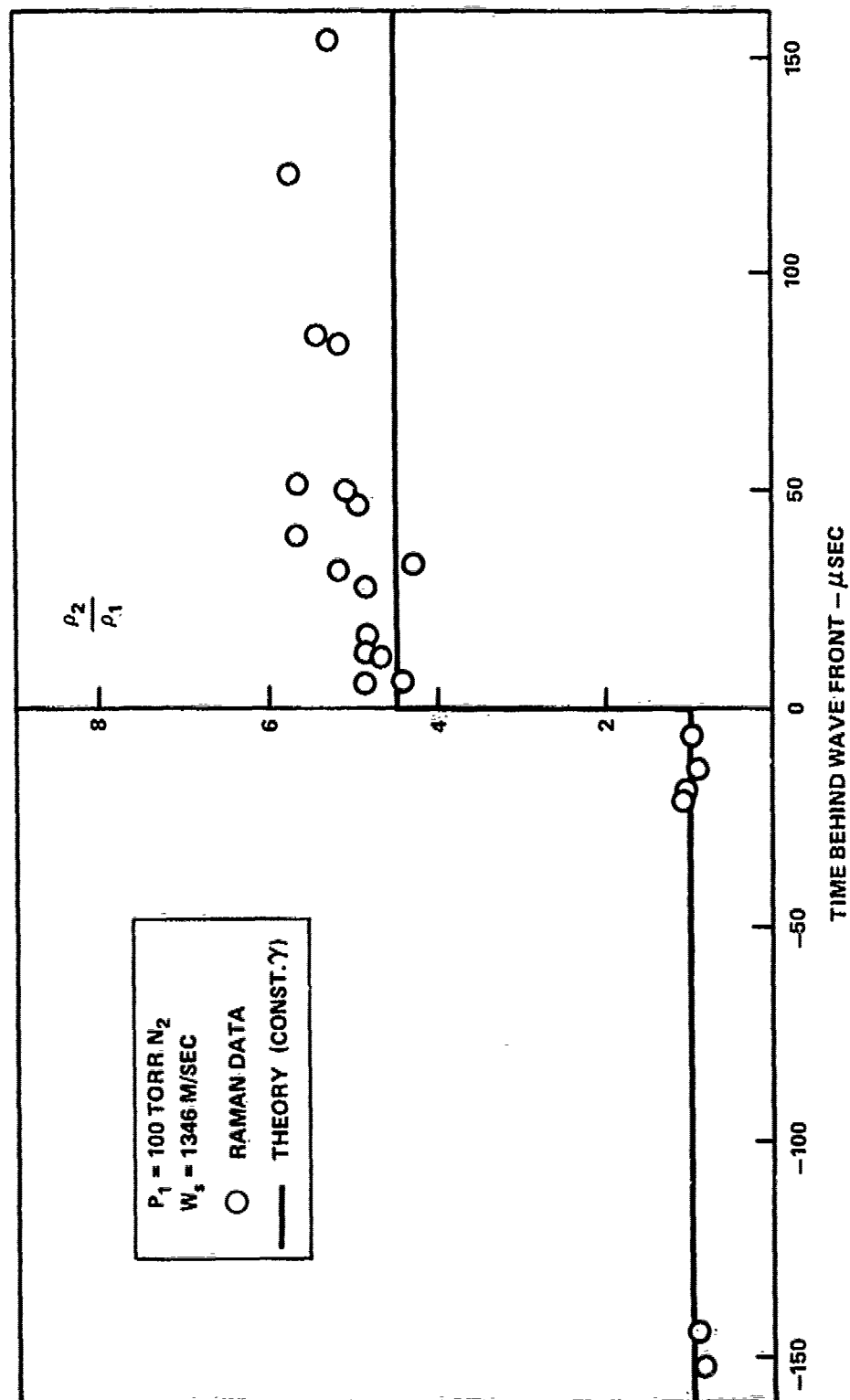


FIG. 12 DENSITY RATIO AS A FUNCTION OF TIME BEHIND THE WAVE FRONT.

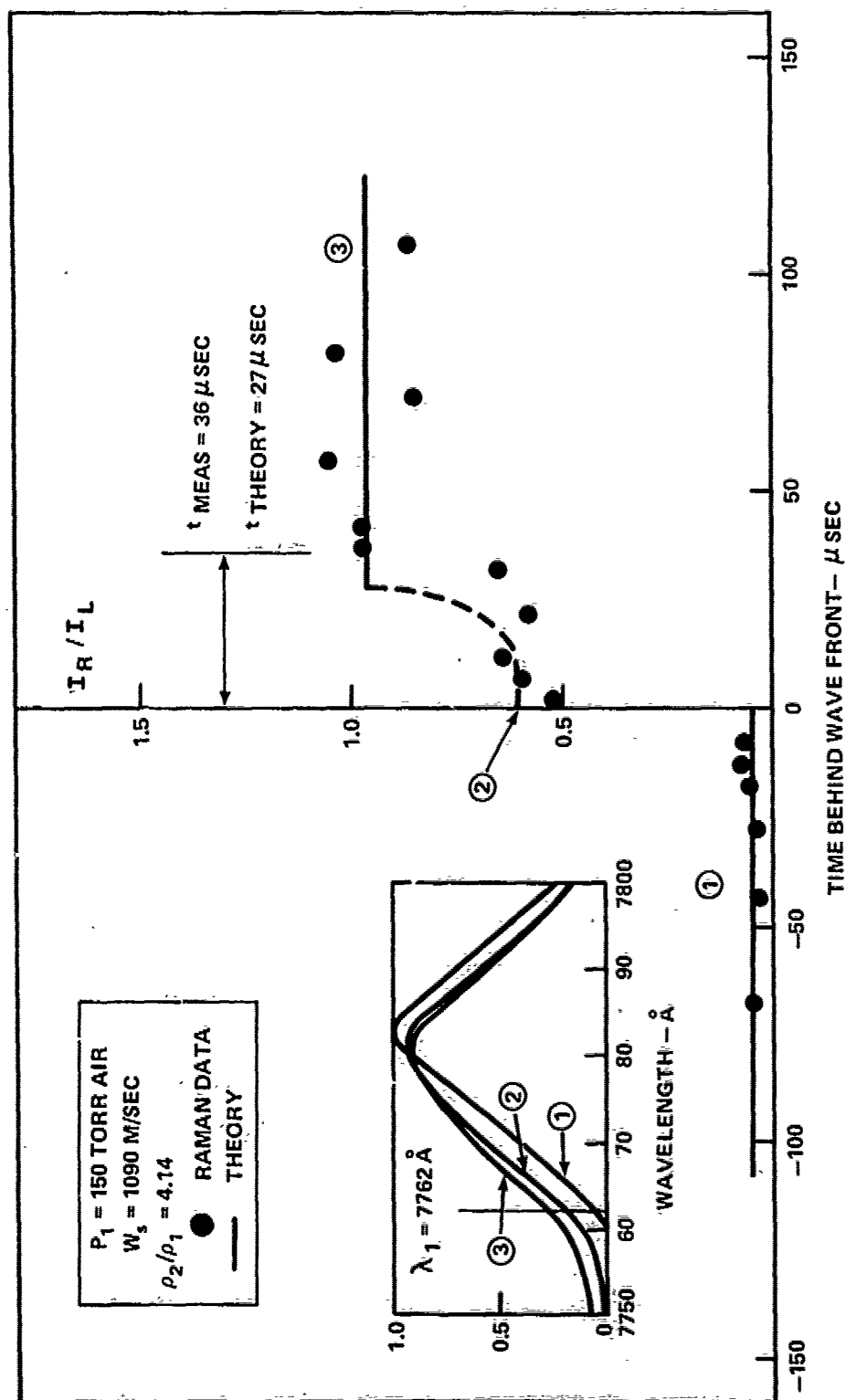


FIG. 13 TIME HISTORY OF RAMAN SCATTERING FROM OXYGEN BEHIND A SHOCK WAVE IN AIR.

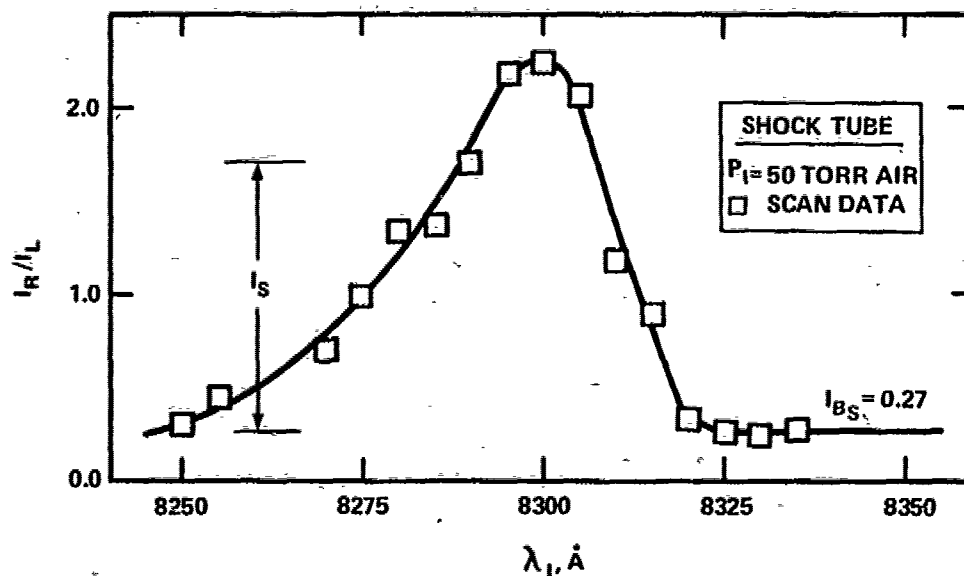
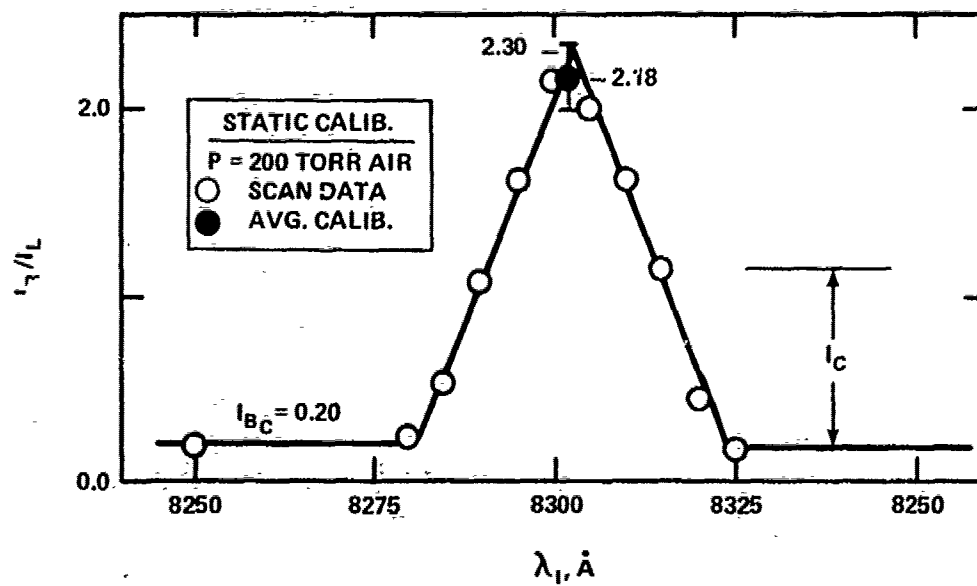


FIG. 14 RAW DATA FOR SCAN METHOD OF DETERMINING DENSITY AND TEMPERATURE USING LRS.

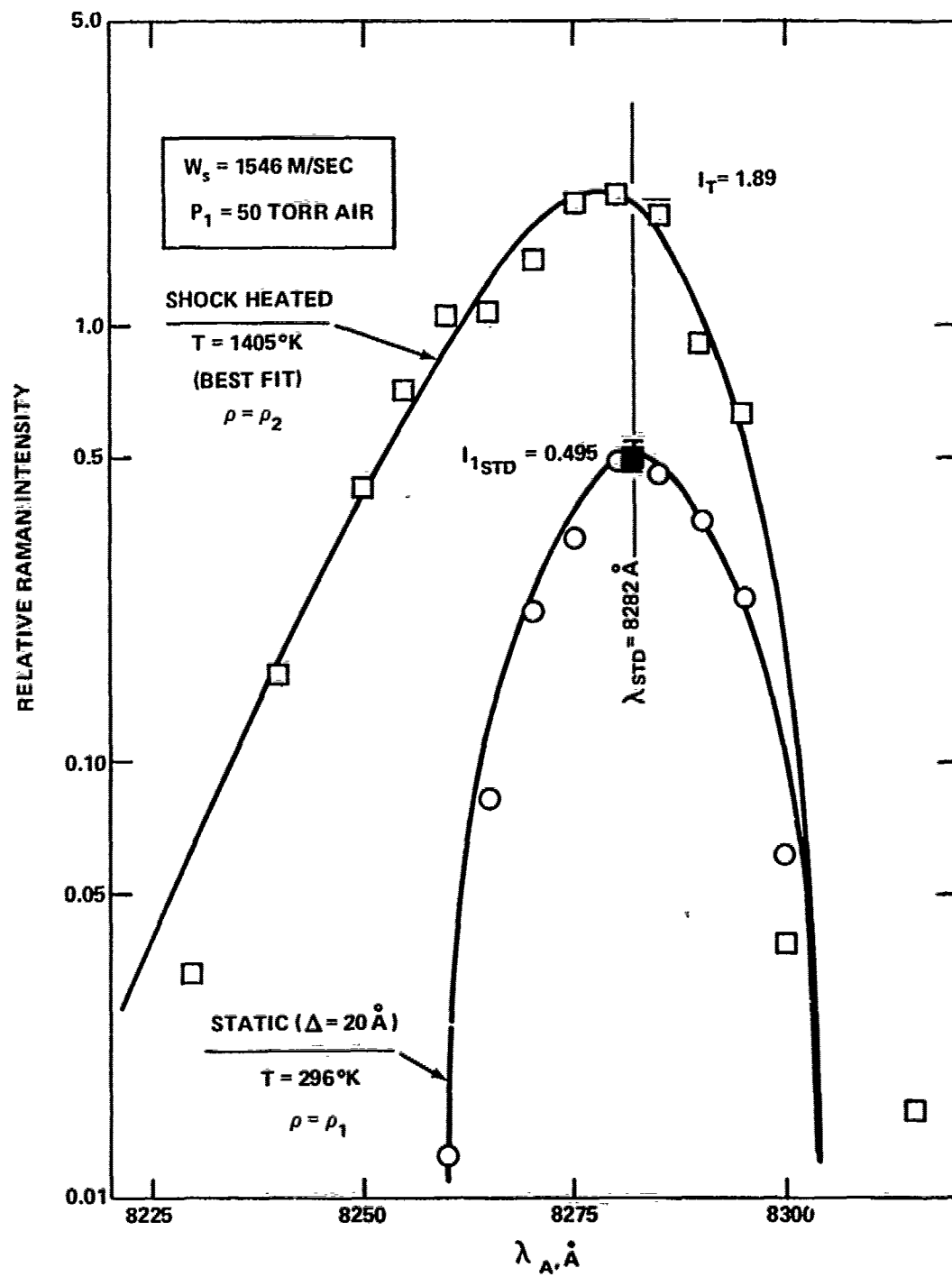


FIG. 15 REDUCED DATA FOR SCAN METHOD OF DETERMINING TEMPERATURE AND DENSITY USING LRS.

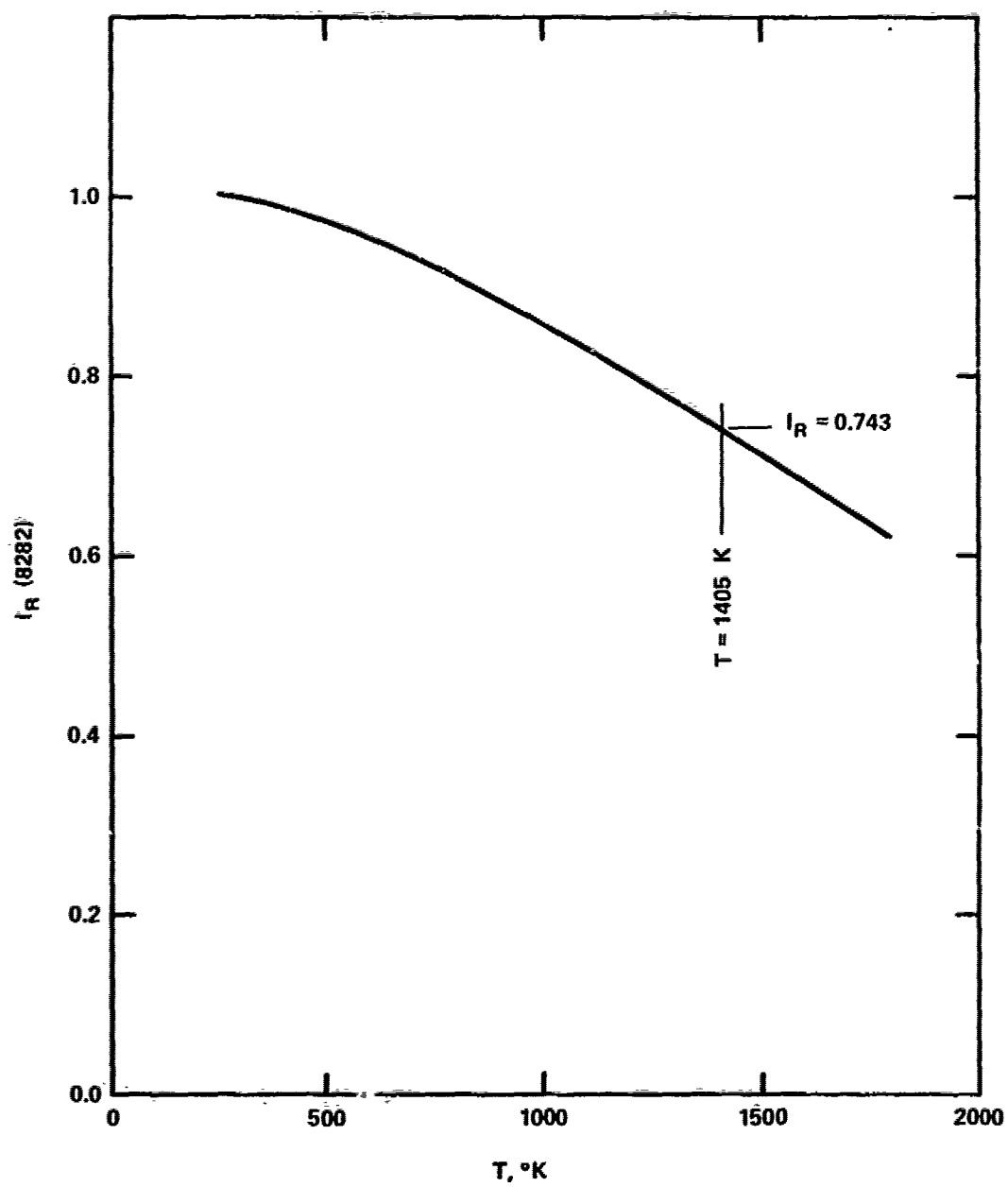


FIG. 16 THEORETICAL CURVE USED TO OBTAIN TEMPERATURE CORRECTION FOR DENSITY DETERMINATION.

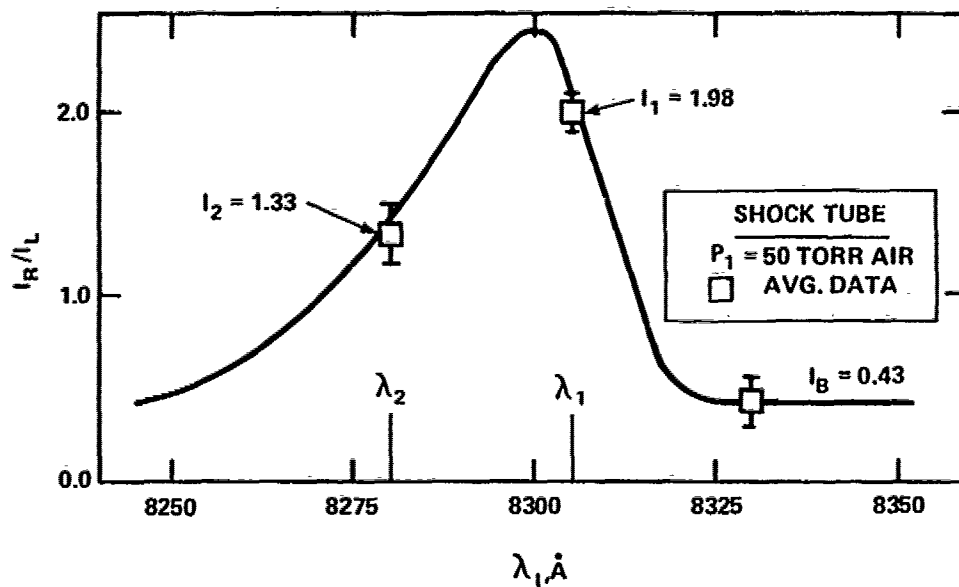
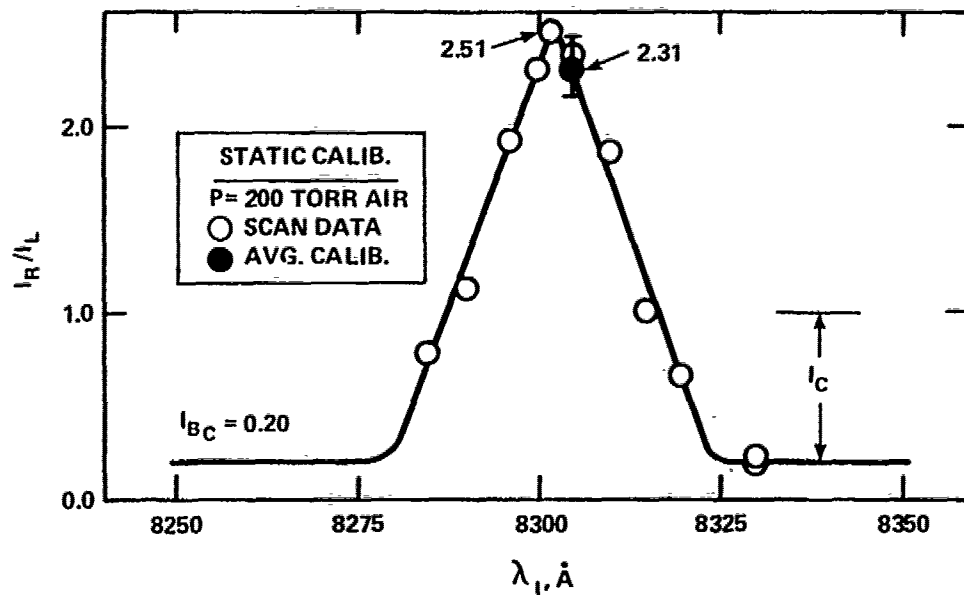


FIG. 17 RAW DATA FOR 2-COLOR METHOD OF DETERMINING DENSITY AND TEMPERATURE USING LRS.

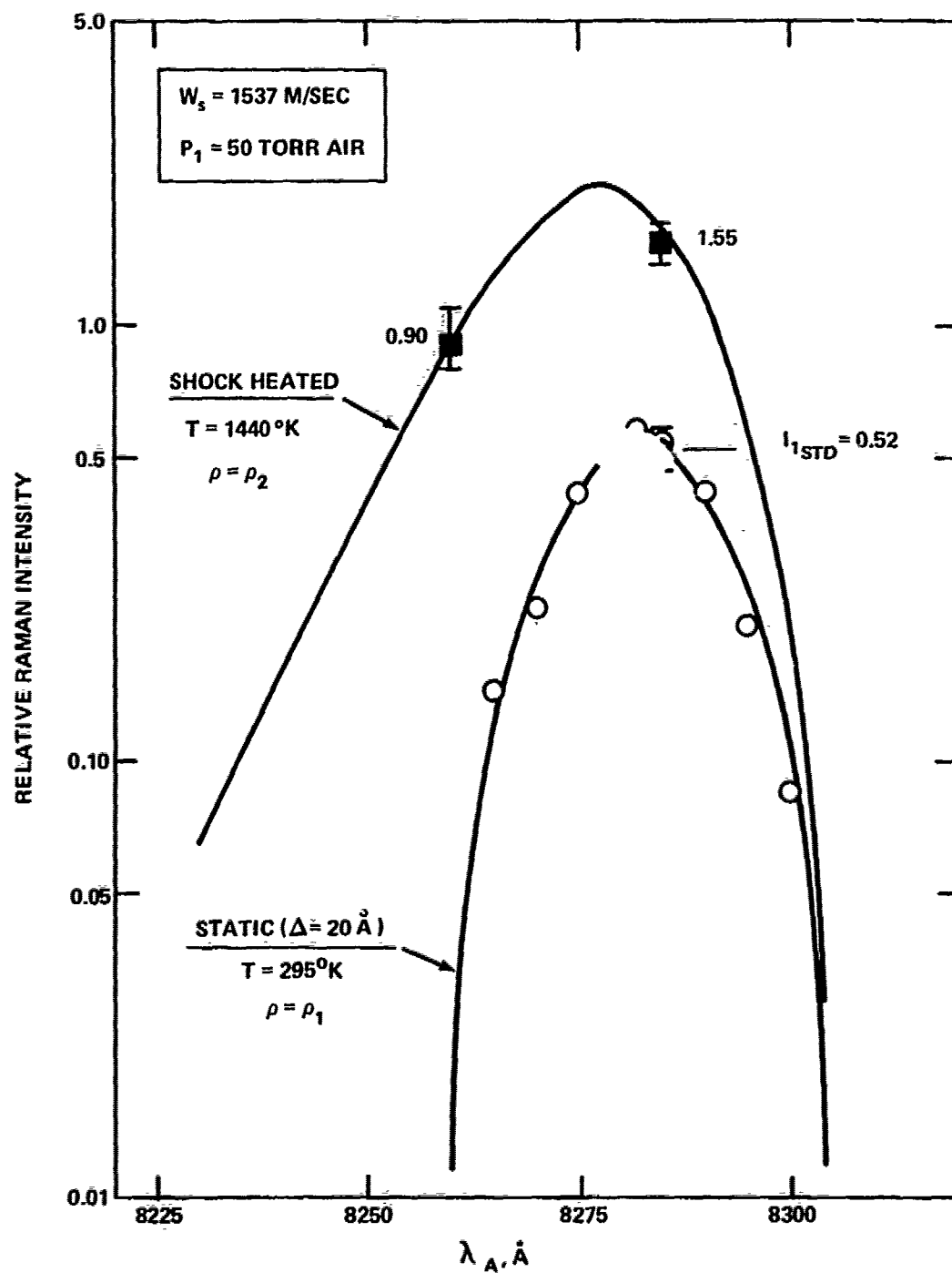


FIG. 18 REDUCED DATA FOR 2-COLOR METHOD OF DETERMINING TEMPERATURE AND DENSITY USING LRS.

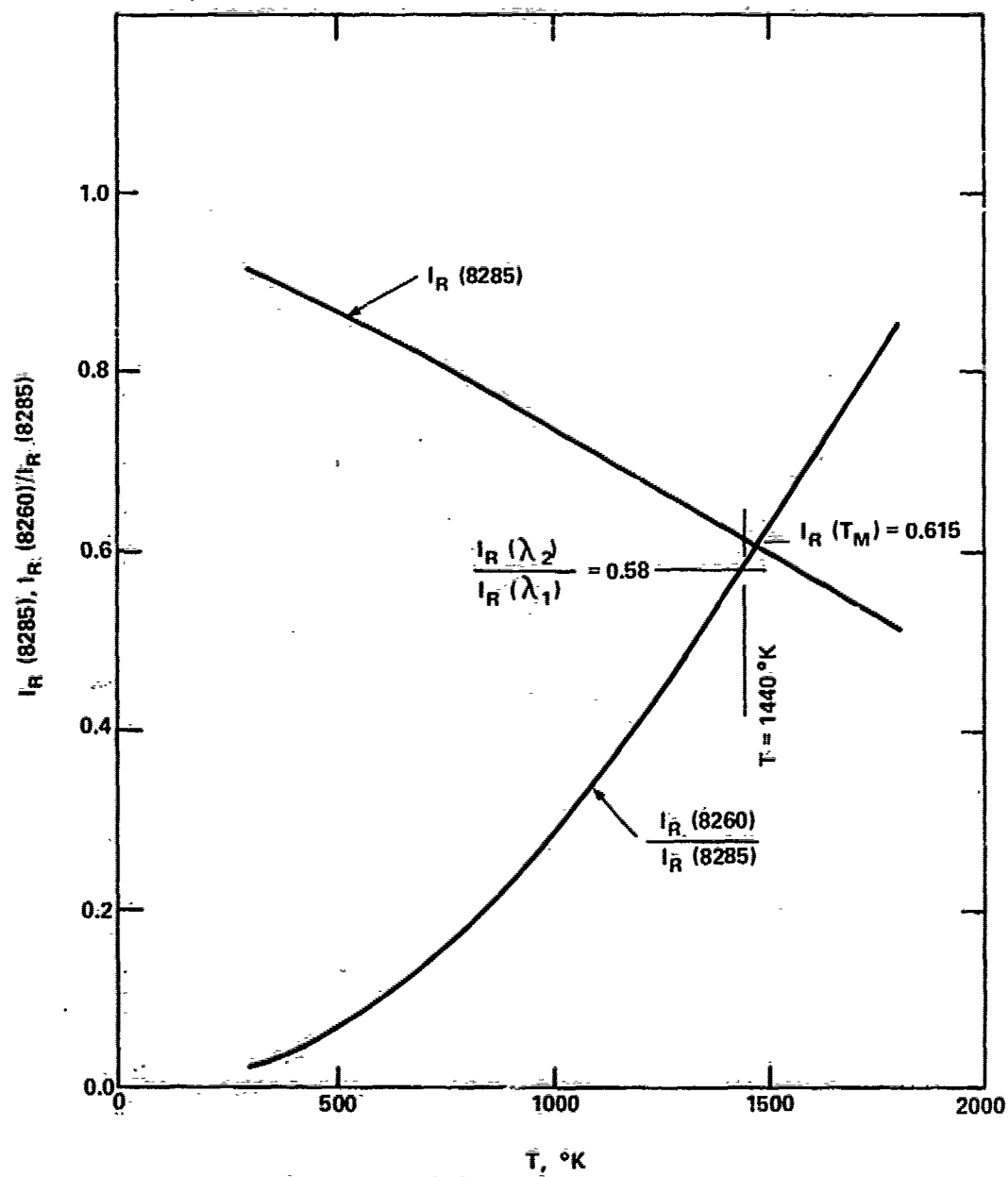


FIG. 19 THEORETICAL CURVES USED TO OBTAIN N₂ TEMPERATURE AND TEMPERATURE CORRECTION FOR DENSITY DETERMINATION

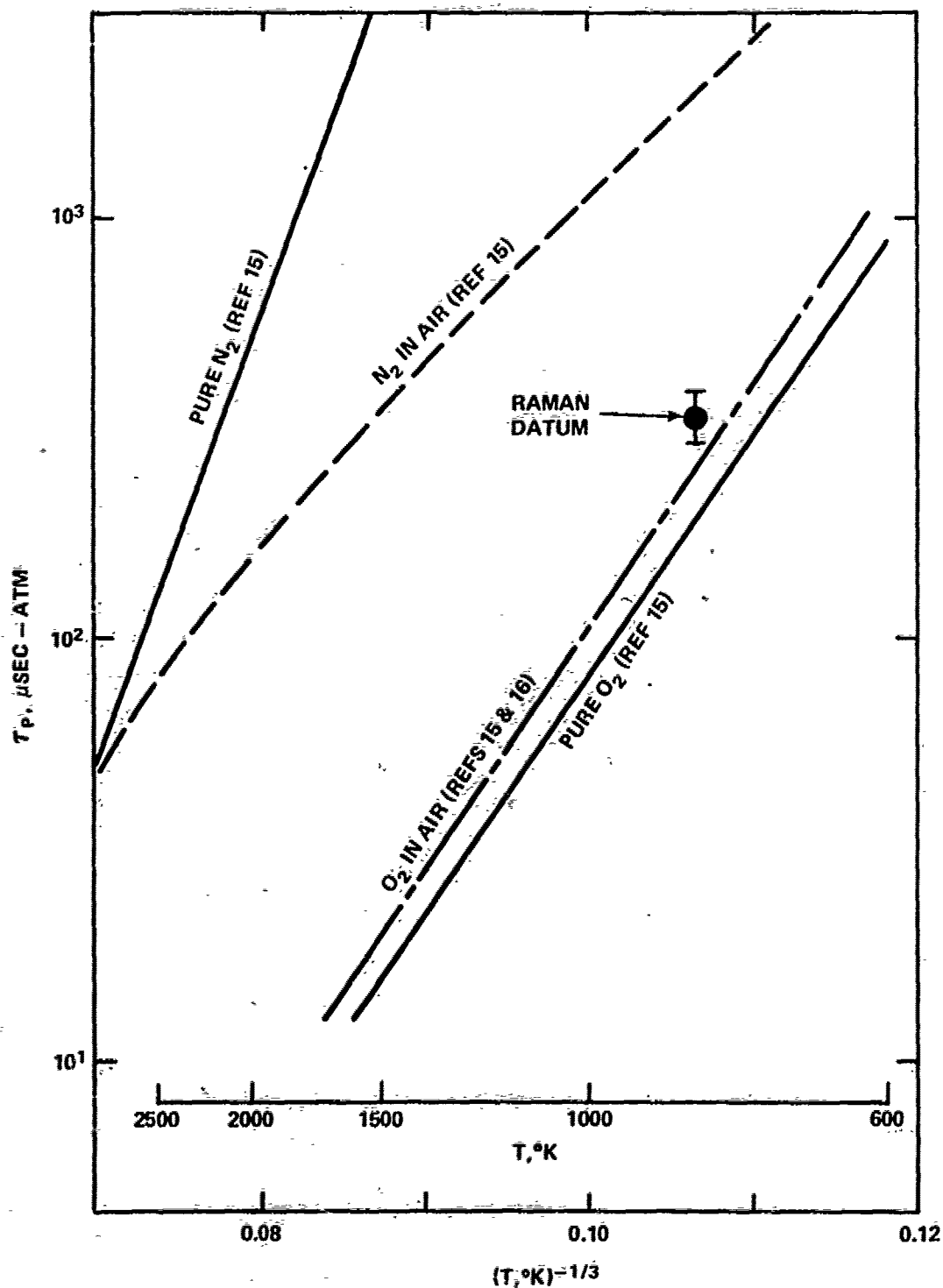


FIG. 20 COMPARISON OF A RAMAN O_2 IN AIR V-T EXCITATION TIME MEASUREMENT WITH OTHER SHOCK-TUBE DATA.

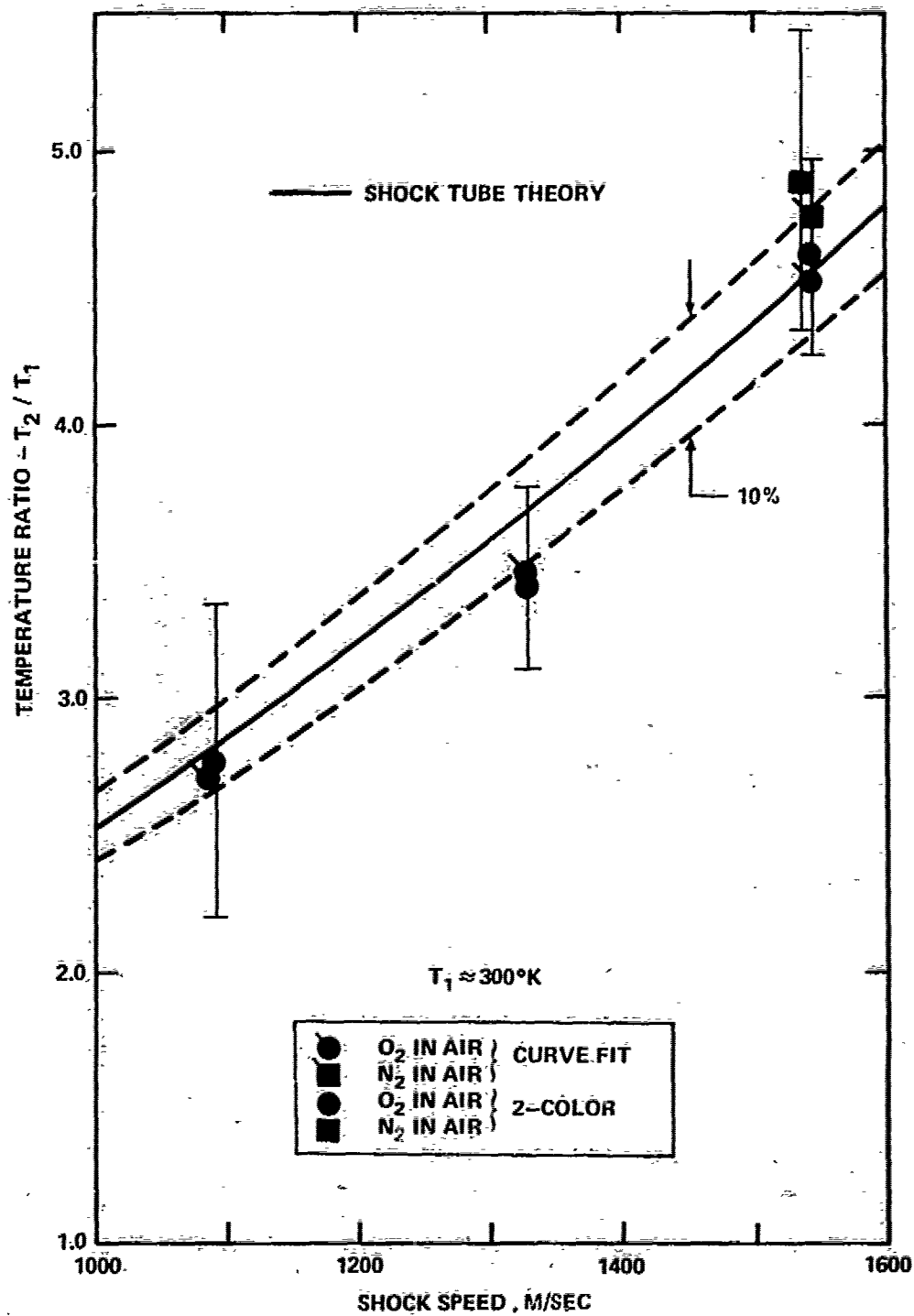


FIG. 21 RAMAN TEMPERATURE RATIO MEASUREMENTS COMPARED TO THEORY FOR O_2 AND N_2 IN SHOCK-HEATED AIR

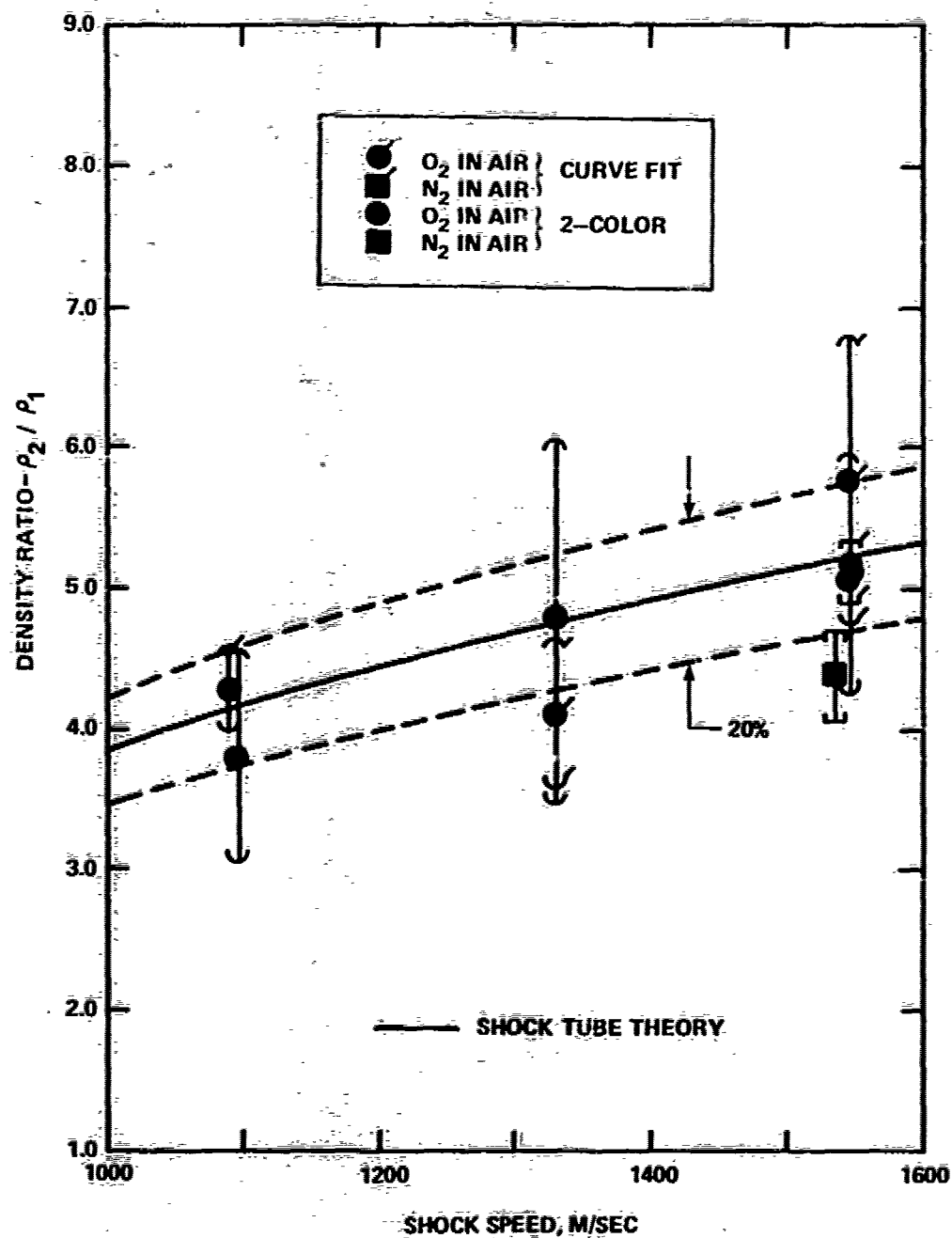


FIG. 22 RAMAN DENSITY RATIO MEASUREMENTS COMPARED TO THEORY FOR O₂ AND N₂ IN SHOCK-HEATED AIR.

AERODYNAMICS DEPARTMENT
DISTRIBUTION
(A1)

Copies		Copies
Commander Naval Sea Systems Command Headquarters Department of the Navy Washington, D. C. 20360 Chief Technical Analyst PMS-405 NSEA-09G32 NSEA-03B	2	Director U. S. Naval Research Laboratory Washington, D. C. 20390 Library Mr. Fred Fluke
Commander Naval Air Systems Command Headquarters Department of the Navy Washington, D. C. 20360 AIR 03B AIR 03C AIR 320 AIR 320C Dr. H. J. Mueller AIR 310 AIR 604	2	NASA Ames Laboratory Moffett Field California 94035 NASA Langley Research Center Langley Station Hampton, Virginia 23365 Lib Aer. ical and Space Me cs Division Dennis Brushwell NASA Lewis Research Center 21000 Brookpark Road Cleveland, Ohio 44135 Library - Mail Stop 60-3 Chief, Wind Tunnel and Flight Division Dr. John W. Dunning, Jr. Mail Stop 500/202 NASA George C. Marshall Space Flight Center Huntsville, Alabama 35812 Mr. T. Reed, R-AERO-AU Mr. W. K. Dahm, R-AERO-A NASA 600 Independence Avenue, S.W. Washington, D. C. 20546 Dr. H. H. Kurzweg, Chief Scientist OAST (Code RR)
Office of Naval Research Department of the Navy Arlington, Virginia 22217 Mr. Morton Cooper Code 430B		
Commanding Officer Naval Ship Research and Development Center Washington, D. C. 20034 Aerodynamics Library (5643)		
Commander Naval Weapons Center China Lake, California 93555 Technical Library (Code 753)		

	Copies		Copies
NASA P. O. Box 33 College Park Maryland 20740		Director of Intelligence Headquarters, USAF (AFNINDE) Washington, D. C. 20330 AFOIN-3B	
NASA Headquarters Washington, D. C. 20546 Mr. F. C. Schwenk Code RD-T		Aerospace Research Laboratories Office of Aerospace Research Wright-Patterson Air Force Base Dayton, Ohio 45433 Thermo-Mechanics Research Laboratory (ARN) Dr. R. H. Korkegi	
Technical Library Director of Defense Research and Engineering (DDR&E) Room 3E-1063, The Pentagon Washington, D. C. 20301 Stop 103		Commander Space and Missile Systems Organization Air Force Unit Post Office Los Angeles Air Force Station California 90045 SMTTM/LT C. Lee	
Defense Documentation Center Cameron Station Alexandria Virginia 22314	12	Headquarters Arnold Engineering Development Center ARO, Incorporated Arnold Air Force Station Tennessee 37389 Library/Documents - Joe Ashley, Jr.	2
Commander (5632.2) Naval Missile Center Point Mugu, California 93041 Technical Library		von Karman Gas Dynamics Facility ARO, Incorporated Arnold Air Force Station Tennessee 37388 Mr. Jack D. Whitfield Chief	
Commanding Officer USA Aberdeen Research and Development Center Aberdeen Proving Ground Maryland 21005 STEAP-TL (Technical Library Division) AMXRD-XSE		Commanding Officer Harry Diamond Laboratories Washington, D. C. 20438 Library, Room 211 Bldg. 92	
Naval Surface Weapons Center Dahlgren laboratory Dahlgren, Virginia 22448 Library Thomas Clare (Code KB)			
Director Strategic Systems Project Office Department of the Navy Washington, D. C. 20390 NSP-2722	2		

Copies

Copies

Commanding General
U. S. Army Missile Command
Redstone Arsenal
Alabama 35809
AMSMI-RR
Chief, Document Section
AMSMI-RDK, Mr. R. A. Deep

Commander (ADL)
Naval Air Development Center
Johnsville, Warminster
Pennsylvania 18974

Commanding Officer
U. S. Air Force Weapons
Laboratory
Technical Library (SUL)
Kirtland Air Force Base
Albuquerque
New Mexico 87117
WLRP
Dr. J. Walsh

U. S. Army Ballistic Missile
Defense Agency
1100 Commonwealth Building
1320 Wilson Boulevard
Arlington, Virginia 22209
Dr. Sidney Alexander

The Johns Hopkins
University (C/NOW 7386)
Applied Physics Laboratory
8621 Georgia Avenue
Silver Spring
Maryland 20910
Document Library
Dr. F. Hill
Dr. L. L. Cronvich

Director
Defense Nuclear
Agency
Headquarters DASA
Washington, D. C. 20305
STSP (STAS)

Commanding Officer
U. S. Army Mobility
Equipment
Research and Development
Center
Fort Belvoir
Virginia 22060
Dr. John W. Bond, Jr.

Commander
Naval Intelligence
Command
Naval Intelligence
Command Headquarters
2461 Eisenhower Avenue
Alexandria, Virginia 22314

Commanding Officer
Naval
Intelligence Support
Center
4301 Suitland Road
Washington, D. C. 20390

Department of Aeronautics
DFAN
USAF Academy
Colorado 80840
COL D. H. Daley, Prof. &
Head

Department of the Army
Office of the Chief of
Research and
Development
ABMDA, The Pentagon
Washington, D. C. 20350

Commanding Officer
Picatinny Arsenal
Dover, New Jersey 07801
Mr. A. A. Loeb
SMUPA-VC-3

Officer-in-Charge
Naval Weapons Center
Corona Annex
Corona, California 91720

Copies

Copies

Commander
Test Command, Defense
Nuclear Agency
Sandia Base, Albuquerque
New Mexico 87115

Commanding Officer
Naval School
Civil Engineer Corps
Officers
Port Hueneme
California 93043

President
Naval War College
Newport, Rhode Island 02840

Superintendent
Naval Postgraduate
School
Monterey
California 93940

Commanding Officer
Naval Damage Control
Training Center
Philadelphia
Pennsylvania 19112
ABC Defense Course

AERODYNAMICS DEPARTMENT
DISTRIBUTION
(A2)

Copies

Aerospace Engineering
Program
University of Alabama
P. O. Box 6307
University of
Alabama 35486
Prof. W. K. Rey, Chem.

AME Department
University of Arizona
Tucson, Arizona 85721
Dr. L. B. Scott

Polytechnic Institute of
Brooklyn
Graduate Center Library
Route 110, Farmingdale
Long Island
New York 11735
Dr. J. Polczynski

Polytechnic Institute of
Brooklyn
Spicer Library
333 Jay Street
Brooklyn, New York 11201
Reference Department

Brown University
Division of Engineering
Providence
Rhode Island 02912
Dr. M. Sibulkin
Library

Copies

California Institute of
Technology
Pasadena
California 91109
Graduate Aeronautical
Laboratories Aero.
Librarian
Dr. H. Liepmann
Karman Lab-301
Prof. L. Lees, Firestone
Flight Science Lab.
Dr. D. Coles,
306 Karman Lab.
Dr. A. Roshko

University of California
Berkeley
California 94720
Dr. M. Holt, Div. of
Aeronautical Sciences
Research Coordinator
College of Engineering

GASDYNAMICS
University of California
Richmond Field Station
1301 South 46th Street
Richmond
California 94804
A. K. Oppenheim

Department of Aerospace
Engineering
University of Southern
California
University Park
Los Angeles
California 90007
Dr. John Laufer

Copies

University of California -
San Diego
Department of Aerospace
and Mechanical
Engineering Sciences
LaJolla
California 92037
Dr. P. A. Libby

Case Western Reserve
University
3306 Clarendon Road
Cleveland, Ohio 44118
G. Kuerti

The Catholic University
of America
Washington, D. C. 20017
Dr. C. C. Chang
Dr. Paul K. Chang
Mechanical Engr. Dept.
Dr. M. J. Casarella
Mechanical Engr. Dept.

University of Cincinnati
Cincinnati, Ohio 45221
Department of Aerospace
Engineering
Dr. Arnold Polak

Department of Aerospace
Engineering Sciences
University of Colorado
Boulder, Colorado 80302

Cornell University
Graduate School of Aero.
Engineering
Ithaca, New York 14850
Prof. W. R. Sears
Dr. S. F. Shen
Prof. F. K. Moore, Head
Thermal Engineering
Dept., 208 Upson Hall

University of Delaware
Mechanical and Aeronautical
Engineering Dept.
Newark, Delaware 19711
Dr. James E. Danberg

Copies

Georgia Institute of
Technology
225 North Avenue, N.W.
Atlanta, Georgia 30332
Dr. Arnold L. Ducoffe
Aerospace Engineering
Dept.

Technical Reports Collection
Gordon McKay Library
Harvard University
Div. of Eng'g. and Applied
Physics
Fierce Hall, Oxford Street
Cambridge
Massachusetts 02138

Illinois Institute of
Technology
3300 South Federal
Chicago, Illinois 60616
Dr. M. V. Morkovin
Prof. A. A. Fejer,
M.A.E. Dept.

University of Illinois
101 Transportation Building
Urbana, Illinois 61801
Aeronautical and Astro-
nautical Engineering
Dept.

Iowa State University
Ames, Iowa 50010
Aerospace Engineering
Dept.

The Johns Hopkins University
Baltimore, Maryland 21218
Prof. S. Corrsin

University of Kentucky
Wenner-Gren Aero. Lab.
Lexington, Kentucky 40506
C. F. Knapp

Copies

Copies

Department of Aero.
Engineering ME 106
Louisiana State
University
Baton Rouge
Louisiana 70803
Dr. P. H. Miller

University of Maryland
College Park
Maryland 20740

Prof. A. Wiley Sherwood
Department of Aerospace
Engineering

Prof. Charles A. Shreeve
Department of Mechanical
Engineering

Dr. S. I. Pai, Institute
of Fluid Dynamics
and Applied
Mathematics

Dr. Redfield W. Allen
Department of
Mechanical Engineering

Dr. W. L. Melnik
Department of
Aerospace Engr.

Dr. John D. Anderson, Jr.
Department of
Aerospace Engineering

Michigan State
University Library
East Lansing, Michigan 48823
Documents Department

Massachusetts Institute of
Technology
Cambridge

Massachusetts 02139

Mr. J. R. Martuccelli
Rm 33-211

Prof. M. Finston

Prof. J. Baron, Dept. of
Aero. and Astro.,
Rm. 37-461

Prof. A. H. Shapiro, Head
Mech. Engr. Dept.

Aero. Engineering Library

Prof. Ronald F. Probestein

Dr. E. E. Covert

Aerophysics Laboratory

University of Michigan
Ann Arbor, Michigan 48104

Dr. A. Kuethe, Dept. of
Aero. Engineering

Dr. M. Sichel, Dept.
of Aero. Engineering

Engineering Library
Aerospace Engineering

Library Aquisitions

Section Serials

Division

Serials and Documents
Section

General Library

University of Michigan
Ann Arbor, Michigan 48104

Mississippi State
University

Department of Aerophysics
and Aerospace Engineering

Drawer AP

Mississippi 39762

Mr. Charles L. Cliett

U. S. Naval Academy
Annapolis, Maryland 21402

Engineering Department,
Aerospace Division

Library, Code 2124

U. S. Naval Postgraduate
School

Monterey

California 93940

Technical Reports
Section

New York University

University Heights

New York, New York 10453

Dr. Antonio Ferri, Director
of Guggenheim Aerospace
Laboratories

Prof. V. Zakkay

Engineering and Science
Library

Copies

North Carolina State
College
Raleigh
North Carolina 27607
Dr. R. W. Truitt, Head,
Mech. and Aero.
Engineering
Dr. H. A. Hassan, Dept.
of Mech. and Aero.
Engineering

D. H. Hill Library
North Carolina State
University
P. O. Box 5007
Raleigh
North Carolina 27607

University of North
Carolina
Chapel Hill
North Carolina 27514
Department of Aero.
Engineering
Library, Documents Section
AFROTC Det 590

Northwestern University
Technological Institute
Evanston, Illinois 60201
Department of Mechanical
Engineering
Library

Dr. John D. Nicolaides
P. O. Box 556
Notre Dame, Indiana 46556

Ohio State University
2036 Neil Avenue
Columbus, Ohio 43210
Aero. Civil Library
Prof. J. D. Lee
Aeronautical Research
Lab.
Prof. G. L. Von Eschen
Dept. of Aero-Astro
Engr.

Copies

Ohio State University
Libraries
Documents Division
1858 Neil Avenue
Columbus, Ohio 43210

Department of Aerospace
Engineering
Room 233 Hammond Building
The Pennsylvania State
University
University Park
Pennsylvania 16802

Pennsylvania State
University Library
Documents Section
University Park
Pennsylvania 16802

Bevier Engineering
Library
126 Benedum Hall
University of
Pittsburgh
Pittsburgh
Pennsylvania 15261
Librarian

Princeton University
James Forrestal Research
Center
Gas Dynamics Laboratory
Princeton, New Jersey 08540
Prof. S. Bogdonoff
Mr. I. E. Vas

Purdue University
School of Aeronautical
and Engineering Sciences
Lafayette, Indiana 47907
Library
Dr. P. S. Lykoudis, Dept.
of Aero. Engineering

Rensselaer Polytechnic
Institute
Troy, New York 12181
Dept. of Aeronautical
Engineering and
Astronautics
Dr. Robert E. Duffy

Copies

Copies

Rutgers - The State
University
University Heights Campus
New Brunswick
New Jersey 08903
Dr. R. H. Page, Dept.
of Mech. and Aero.
Engineering

2

Stanford University
Stanford
California 94305
Librarian, Dept. of
Aeronautics and
Astronautics

Stevens Institute of
Technology
Hoboken, New Jersey 07030
Mechanical Engineering
Department
Library

The University of Texas
at Austin
Applied Research
Laboratories
P. O. Box 8029
Austin, Texas 78712
Director

University of Toledo
Department of Aero.
Engineering
Research Foundation
Toledo, Ohio 43606

Documents Department
Virginia Polytechnic
Institute
Blacksburg
Virginia 24061
Carol M. Newman
Library

University of Virginia
Charlottesville
Virginia 22901
Alderman Library
Science Reference
Division
Dr. G. Matthews, Dept.
of Aerospace
Engineering

University of Washington
Seattle, Washington 98105
Engineering Library
Dept. of Aeronautics
and Astronautics
Prof. K. E. Street, Dept.
of Aero. and Astro.
Prof. A. Hertzberg, Aero.
and Astro. Guggenheim
Hall

West Virginia University
Morgantown
West Virginia 26506
Library

Federal Reports Center
University of Wisconsin
462 Mechanical Engineering
Building
1513 University Avenue
Madison, Wisconsin 53706
S. Reilly
J. S. Murphy

Los Alamos Scientific
Laboratory
P. O. Box 1663
Los Alamos, New Mexico 87544
Report Library

Copies

University of Maryland
Baltimore County (UMBC)
5401 Wilkens Avenue
Baltimore
Maryland 21228
Dr. R. C. Roberts
Mathematics Dept.

Oklahoma State University
Office of Engineering
Research
Stillwater
Oklahoma 74074
Dr. V. S. Haneman, Jr.

Institute for Defense
Analyses
400 Army-Navy Drive
Arlington
Virginia 22202
Classified Library

Kaman Nuclear
1700 Garden of the
Gods Road
Colorado Springs
Colorado 80907

Kaman Science Corporation
Avidyne Division
83 Second Avenue
Burlington
Massachusetts 01803
Dr. J. R. Ruetenik

Rockwell International
B-1 Division
International Airport
Technical Information Center
(BA08)
Los Angeles, California 90009
LAD Library, Dept. 299

Copies

North American Rockwell
Corporation
Engineering Data Services
4300 E. Fifth Avenue
Columbus, Ohio 43216

M.I.T. Lincoln Laboratory
P. O. Box 73
Lexington
Massachusetts 02173
Library A-082
Dr. S. Edelberg
Dr. R. H. Kingston
Mr. J. Freedman
Dr. G. P. Dinneen
Dr. R. H. Rediker

The RAND Corporation
1700 Main Street
Santa Monica
California 90406
Library - D

The Boeing Company
P. O. Box 3999
Seattle
Washington 98124
Aerospace Library
8K-38 J. M. MacDonald

United Aircraft Corporation
Research Laboratories
East Hartford
Connecticut 06108
Dr. William M. Foley

United Aircraft Corporation
400 Main Street
East Hartford
Connecticut 06108
Library

Hughes Aircraft Company
Continela and Teale Streets
Culver City
California 90230
Co. Tech. Doc. Ctr.,
MS 6/E110

Copies

Copies

Lockheed Missiles and
Space Company
3251 Hanover
Palo Alto
California 94304
H. S. Bettencourt
Dept. 81-11
Bldg. 154
L. R. Lunsford
Orgn. 52-24
Bldg. 201

Lockheed Missiles and
Space Company
3251 Hanover Street
Palo Alto
California 94304
Technical Information
Center

Lockheed-California
Company
Burbank
California 91503
Central Library
Dept. 84-40
Bldg. 170, PLT. B-1

Vice President and
Chief Scientist
Dept. 03-01

Lockheed Aircraft
Corporation
P. O. Box 551
Burbank
California 91520
Dr. Ronald Smelt

Martin Marietta Corporation
P. O. Box 988
Baltimore
Maryland 21203
Science-Technology
Library (Mail No. 398)

Martin Company
3211 Trade Winds Trail
Orlando, Florida 32805
Mr. H. J. Diebolt

General Dynamics
P. O. Box 748
Fort Worth, Texas 76101
Research Library
2246
George Kaler, Mail
Zone 2880

Cornell Aeronautical
Laboratory, Inc.
4455 Genesee Street
Buffalo, New York 14221
Library

Air University Library
(SE) 63-578
Maxwell Air Force Base
Alabama 36112

McDonnell Douglas
Corporation
Research & Engineering
Library
Dept. 209, Bldg. 33
P. O. Box 516
St. Louis
Missouri 63166

McDonnell Douglas
Astronautics Company
Space Systems Center
5301 Bolsa Avenue
Huntington Beach
California 90405
A2-260 Library
Dr. J. S. Murphy, A-830
Mr. W. H. Branch, Director
A3-339 Library
P. L. Klenatt A3-833

Copies

Copies

Fairchild Hiller
Republic Aviation
Division
Farmingdale
New York 11735
Engineering Library

General Applied Science
Laboratories, Inc.
Merrick and Stewart
Avenues
Westbury, Long Island
New York 11590
Dr. F. Lane

The Whitney Library
General Electric Research
and Development Center
The Knolls, K-1
P. O. Box 8
Schenectady
New York 12301
M. F. Orr, Manager

General Electric Company
Missile and Space
Division
P. O. Box 8555
Philadelphia
Pennsylvania 19101
MSD Library
Larry Chasen, Mgr.
Dr. J. D. Stewart, Mgr.
Research and Engineering

General Electric Company
AEG Technical Information
Center N-32
Cincinnati, Ohio 45215

General Electric Company
Missile and Space
Division
P. O. Box 8555
Philadelphia
Pennsylvania 19101
Dr. S. M. Scala
Dr. H. Lew
Mr. J. W. Faust
Mr. W. Daskin
S. B. Kottok
S. Kahn
J. B. Arnaiz
L. A. Marshall
A. Martellucci

AVCO-Everett Research
Laboratory
2385 Revere Beach Parkway
Everett
Massachusetts 02149
Library
Dr. George Sutton

LTV Aerospace Corporation
Vought Systems Division
P. O. Box 5907
Dallas, Texas 75222
Mr. F. G. Simpson
Mail Station 2-54142

2

LTV Aerospace Corporation
Missiles and Space Division
P. O. Box 6267
Dallas, Texas 75222
MSD-T-Library

Northrop Norair
3901 West Broadway
Hawthorne
California 90250
Tech. Info. 3343-32

Grumman Aircraft Engineering
Corporation
Bethpage, Long Island
New York 11714
Mr. R. A. Scheuing
Mr. H. B. Hopkins
Mr. H. R. Reed

Copies

Copies

Marquardt Air/raft
Corporation
16555 Saticoy Street
Van Nuys
California 91409
Library

ARDE Associates
P. O. Box 286
580 Winters Avenue
Paramus, New Jersey 07652
Librarian

Aeronautical Research
Associates of
Princeton
50 Washington Road
Princeton, New Jersey 08540
Dr. C. duP. Donaldson

General Research Corporation
5383 Hollister Avenue
P. O. Box 3587
Santa Barbara
California 93105
Technical Info. Officer

Sandia Corporation
Sandia Base
Albuquerque
New Mexico 87115
Mr. K. Goin, Div. 9322
Mrs. B. R. Allen
Div 3421

HERCULES INCORPORATED
Allegany Ballistics
Laboratory
P. O. Box 210
Cumberland
Maryland 21502
Mrs. Louise E. Derrick
Librarian

General Electric Company
P. O. Box 2500
Daytona Beach
Florida 32015
Dave Hovis, Rm. 4109

TRW Systems Group
1 Space Park
Redondo Beach
California 90278
Technical Library-
Document
Acquisitions

Stanford Research
Institute
333 Ravenswood Avenue
Menlo Park
California 94025
Dr. G. Abrahamson
Mr. John Malick L3088

Hughes Aircraft Company
P. O. Box 3310
Bldg. 300/MSE-245
Fullerton
California 92634
R. H. Sterling, 600-E201

Westinghouse Electric
Corporation
Astronuclear Laboratory
P. O. Box 10864
Pittsburgh
Pennsylvania 15236
Library

CONVAIR Division of General
Dynamics
Library and Information
Services
P. O. Box 12009
San Diego
California 92112

CONVAIR Division of
General Dynamics
P. O. Box 1128
San Diego
California 92112
Dr. Jan Raat, Aero-
ballistics
Dept. Mail Zone 583-00

Copies

Copies

AVCO Missiles Systems
Division
201 Lowell Street
Wilmington
Massachusetts 01887
E. E. H. Schurmann
J. Otis

Chrysler Corporation
Space Division
P. O. Box 29200
New Orleans
Louisiana 70129
G. T. Boyd, Dept. 2781

General Dynamics
Pomona Division
Pomona, California 91766
Division Library
Mail Zone 6-20

Philco-Ford Corporation
Aeroneutronic Division
Newport Beach
California 92660
Dr. A. Demetriades

Raytheon Company
Missile Systems Division
Hartwell Road
Bedford
Massachusetts 01730
Dr. H. A. Mehlhorn
Optical Systems
Dept. (S4-55)

TRW Systems Group
Space Park Drive
Houston, Texas 77058
M. W. Sweeney, Jr.

Marine Bioscience
Laboratory
527 Las Alturas Road
Santa Barbara
California 93103
Dr. A. C. Charters

University of Wyoming
Laramie, Wyoming 82070
Library
Prof. Matheny

ELMAC, Division Varian
Associates
301 Industrial Way
San Carlos
California 94070
J. R. Quinn, Marketing
Manager

The Aerospace Corporation
P. O. Box 92957
Los Angeles
California 90009
Dr. W. R. Warren, Jr.
130/691

Department of the Air Force
Headquarters Air Force
Special Communications
Center
San Antonio
Texas 78243

HP/EGL PROGRAM REPORTS DISTRIBUTION
LIST "B" TECHNICAL REPORTS

Copies	Copies
<p>Defense Advanced Research Projects Agency 1400 Wilson Boulevard Arlington Virginia 22209 Director, Laser Division</p>	<p>National Aeronautics and Space Administration Ames Research Center Moffett Field California 94035 Mr. Robert L McKenzie Dr. Kenneth W. Billman</p> <p style="text-align: right;">2</p>
<p>ODDR&E Pentagon Washington, D. C. 20301 Assistant Director (Space and Advanced Systems)</p>	<p>National Security Agency Fort George G. Meade Maryland 20755 Mr. Richard C. Foss A763 FANX III</p>
<p>U. S. Arms Control and Disarmament Agency Department of State Building, Room 4931 Washington, D. C. 20451 Dr. Charles Henkin</p>	<p>Department of the Army Office of the Chief, R&D Washington, D. C. 20310 DARD-ARS-P (Mr. A. L. Stoessell) DARD-DD</p> <p style="text-align: right;">2</p>
<p>National Aeronautics and Space Administration Code RR, ROB 10B 600 Independence Avenue, S.W. Washington, D. C. 20546</p>	<p>Department of the Army Office of the Assistant Chief of Staff for Force Dev. Washington, D. C. 20310 DAFD-AD (MAJ Bradley) DAFD-SDF (LTC Bryan)</p> <p style="text-align: right;">2</p>
<p>Division of Military Applications Energy Research and Development Administration Washington, D. C. 20545 Dr. Lawrence Killion</p>	<p>U. S. Army SAFEGUARD System Office The Commonwealth Building 1300 Wilson Boulevard Arlington, Virginia 22209 Mr. Al J. Bast, Jr.</p> <p style="text-align: right;">3</p>
<p>National Aeronautics and Space Administration Lewis Research Center Cleveland, Ohio 44135 Dr. John W. Dunning, Jr. (Aerospace Res. Engineer)</p>	<p>Director U. S. Army Advanced Ballistic Missile Defense Agency 1300 Wilson Boulevard Commonwealth Building Arlington, Virginia 22209 RDMC-NC, Mr. M. Zlotnick</p>

Copies

Commander
U. S. Army Missile Command
Redstone Arsenal
Alabama 35809
Army High Energy Laser
Programs
Walter B. Jennings, Jr. 3

Commander
Rock Island Arsenal
Rock Island
Illinois 61201
SARRI-LR
Mr. J. W. McGarvey

Commanding Officer
U. S. Army Mobility Equipment
R&D Center
Ft. Belvoir
Virginia 22060
SMEFB-MW

Commander
U. S. Army Missile Command
Redstone Arsenal
Alabama 35809
AMSMI-RNS

Director
Ballistic Missile Defense
Advanced Technology Center
P. O. Box 1500
Huntsville
Alabama 35807
ATC-O
ATC-M, Dr. B. Shratter
ATC-T
Mr. J. Hagefstration 3

Commander
U. S. Army Materiel Command
5001 Eisenhower Avenue
Alexandria, Virginia 22304
AMCRD-T (Dr. David Stefanye)
(Mr. Paul Chernoff)
(Dr. B. Zarwyn) 3

Copies

Commander
U. S. Army Armament
Command
Rock Island
Illinois 61201
AMSAR-RDT

Director
U. S. Army Ballistic
Res. Laboratory
Aberdeen Proving Ground
Maryland 21005
Dr. Robert Eichelberger
Mr. Frank Allen
Dr. F. C. Alcaez 3

Commandant
U. S. Army Air Defense
School
Ft. Bliss, Texas 79916
Air Defense Agency

Commandant
U. S. Army Air Defense
School
Ft. Bliss, Texas 79916
ATSA-CTD-MS
(CAPT Poage)

Commander
U. S. Army Training and
Doctrine Command
Ft. Monroe
Virginia 23651
ATCD-CF

Commander
USA Frankford Arsenal
Building 201-3
Bridge & Tacony Streets
Philadelphia
Pennsylvania 19137
Mr. M. Elnick
(SARFA-FCD)

Commander
U. S. Army Electronics
Command
Ft. Monmouth
New Jersey 07703
AMSEL-CT-L (Dr. R. G. Buser)

Copies

Commander
U. S. Army Combined Arms
Combat Developments
Activity
Fort Leavenworth
Kansas 66027

Deputy Commandant for
Combat and Training
Developments
U. S. Army Ordnance Center
and School
Aberdeen Proving Ground
Maryland 21005
ATSL-CTD-MS-R (LTC Stewart)

Department of the Navy
Office of the Chief of Naval
Operations
Pentagon 5C743
Washington, D. C. 20380
CAPT M. T. Greeley, USN
(OP-982F3)

Office of Naval Research
495 Summer St.
Boston
Massachusetts 02110
Dr. Fred Quelle

Office of Naval Research
800 North Quincy Street
Arlington
Virginia 22217
Dr. W. J. Condell (421)

Department of the Navy
Deputy Chief of Naval
Materiel (Dev.)
Washington, D. C. 20360
Mr. R. Gaylord (MAT 032B)

Naval Missile Center
Point Mugu
California 93042
Gary Gibbs (Code 5352)

Copies

Commander
Naval Sea Systems
Command
Department of the Navy
Washington, D. C. 20360
CAPT J. G. Wilson,
PMS -405

Naval Research Laboratory
Washington, D. C. 20375
Dr. W. R. Sooy
(Code 5503) EOTPO
Dr. P. Livingston
(Code 5560)
Dr. H. Shenker
(Code 5507)
Mr. D. J. McLaughlin
(Code 5560)
Dr. J. L. Walsh
(Code 5503)
Dr. J. I. Connolly, Jr.
(Code 5503C)
Dr. J. T. Schriempf
(Code 6330)
Dr. R. F. Wenzel
(Code 6461)
Mr. R. W. Rice
(Code 6130)

Superintendent
Naval Postgraduate School
Monterey
California 93940
Library (Code 2124)

10

Copies

Copies

U. S. Naval Weapons Center
China Lake
California 93555
Mr. E. B. Niccum (Code 5114)

Hq. AFSC/XRLW
Andrews AFB
Washington, D. C. 20331
CAPT E. H. Cobb

Hq. USAF(RDPS)
Washington, D. C. 20330
LTCOL A. J. Chiota

Hq. AFSC(DLCAW)
Andrews AFB
Washington, D. C. 20331
MAJ H. Axelrod

Air Force Weapons Laboratory
Kirtland AFB
New Mexico 87117
COL Donald L. Lamberson (AR)
COL John C. Scholtz (PG)
CAPT Dale Holmes (LRD)
MAJ Chet Deane

Hq. SAMSO
P. O. Box 92960
Worldway Postal Center
Los Angeles
California 90009
CAPT Dorian A. DeMaio
(XRTD)
IND

AF Avionics Laboratory (TEL)
Wright Patterson AFB
Ohio 45433
Mr. K. Hutchinson

AF Materials Laboratory (LPL)
Wright Patterson AFB
Ohio 45433
MAJ William Goldberg

Department of the Air Force
Hq. Foreign Technology
Division
Wright Patterson AFB
Ohio 45433
PDTN

RADC
Griffiss AFB
New York 13441
(OCSE/Mr. R. Urtz)

Hq. Electronics Systems
F vision (ESL)
L. J. Hanscom Field
Bedford
Massachusetts 01730
Mr. Alfred E. Anderson
(XRP)

AF Rocket Propulsion
Laboratory
Edwards AFB
California 93523
B. R. Bornhorst (LKCG)

AF Aerospace Propulsion
Laboratory
Wright Patterson AFB
Ohio 45433
COL Walter Moe (CC)
PDTR

CINCSAC/INEP
Offutt AFB
Nevada 68113

USAF/INAKA
Washington, D. C. 20330
LTCOL W. M. Truesdell

Defense Intelligence Agency
Washington, D. C. 20301
Mr. Seymour Berler (DTIB)

Central Intelligence Agency
Washington, D. C. 20505
Mr. Julian C. Nall

	Copies		Copies
Analytic Services, Incorporated 5613 Leesburg Pike Falls Church Virginia 22041 Dr. John Davis		Boeing Company P. O. Box 3999 Seattle, Washington 98124 Mr. M. I. Gamble Ordn 2-1460, MS 8C-88	2
Aerospace Corporation P. O. Box 92957 Los Angeles California 90009 Dr. G. P. Millburn Dr. Walter Warren	2	ESI, Incorporated 495 Java Drive Sunnyvale California 94086 Arthur Einhorn	
The Garrett Corporation Airesearch Manufacturing Company 9851 Sepulveda Boulevard Los Angeles California 90009 Mr. A. Colin Stancliffe		Xerox Corporation Electro-Optical Systems 300 North Halstead Pasadena California 91107 Dr. Andrew Jensen	
Atlantic Research Corporation Shirley Highway at Edsall Road Alexandria Virginia 22314 Mr. Robert Naismith		General Electric Co. P. O. Box 8555 Philadelphia Pennsylvania 19101 Mr. W. J. East Dr. C. E. Anderson Dr. R. R. Sigismonti	3
AVCO - Everitt Research Laboratory 2385 Revere Beach Parkway Everett Massachusetts 02149 Dr. George Sutton Dr. Jack Dougherty	2	General Electric Company 100 Plastics Avenue Pittsfield Massachusetts 01201 Mr. D. G. Harrington Room 1044	
Battelle Columbus Laboratories 505 King Avenue Columbus, Ohio 43201 Mr. Fred Tietzel (STOIAIC)		General Research Corporation P. O. Box 3587 Santa Barbara California 93105 Dr. R. Holbrook	
Bell Aerospace Company Division of Textron, Incorporated P. O. Box 1 Buffalo, New York 14240 Dr. Wayne C. Solomon		General Research Corporation 1501 Wilson Boulevard, Suite 700 Arlington Virginia 22209 Dr. Giles F. Crimi	

Copies	Copies
<p>Hercules, Incorporated Industrial Systems Department 910 Market Street Wilmington Delaware 19899 Mr. J. E. Greer Director, Systems Group</p>	<p>Johns Hopkins University Applied Physics Laboratory 8621 Georgia Avenue Silver Spring Maryland 20910 Dr. Albert M. Stone Dr. R. E. Gorozdos</p>
<p>Hercules, Incorporated P. O. Box 210 Cumberland Maryland 21502 Dr. Ralph F. Preckel</p>	<p>Lawrence Livermore Laboratory P. O. Box 808 Livermore California 94550 Dr. R. E. Kidder Dr. E. Teller Dr. Joe Fleck Dr. John Emmett Mr. Carl Haussmann</p>
<p>Hughes Research Laboratories 3011 Malibu Canyon Road Malibu, California 90265 Dr. D. Forster Dr. Arthur N. Chester</p>	<p>Los Alamos Scientific Laboratory P. O. Box 1663 Los Alamos New Mexico 87544 Dr. Keith Boyer</p>
<p>Hughes Aircraft Company Aerospace Group - Systems Division Canoga Park California 91304 Dr. Jack A. Alcalay</p>	<p>Lulejian and Associates, Incorporated Del Amo Financial Center Suite 500 21515 Hawthorne Boulevard Torrance California 9050</p>
<p>Hughes Aircraft Company Centinela and Teale Streets Culver City California 90230 Dr. Eugene Peressini (Building 6, MS/E-125) Dr. John Fitts (MS 5/B-138)</p>	<p>Lockheed Palo Alto Research Laboratory 3251 Hanover Street Palo Alto California 94304 L. R. Lunsford Orgn. 52-24, Bldg. 201</p>
<p>Hughes Aircraft Company P. O. Box 3310 Fullerton California 90230 Dr. William Yates</p>	<p>Mathematical Sciences Northwest, Incorporated 4545-15th Avenue, N. E. Seattle Washington 98105 Mr. Peter H. Rose Dr. Abraham Hertzberg</p>
<p>Institute for Defense Analyses 400 Army Navy Drive Arlington Virginia 22202 Dr. Alvin Schnitzler</p>	

Copies

Copies

Martin Marietta Aerospace
P. O. Box 179
Denver, Colorado 80201
Mr. Stewart Chapin
(Mail No. 0445)
Dr. Scott Gilles
(Mail No. C2006)

2

Massachusetts Institute
of Technology
Lincoln Laboratory
Lexington
Massachusetts 02173
Dr. S. Edelberg
Dr. L. C. Marquet
Dr. J. Freedman
Dr. G. P. Dinneen
Dr. R. H. Rediker

5

McDonnell Douglass
Astronautics Company
5301 Bolsa Avenue
Huntington Beach
California 92647
Mr. P. L. Klevatt
Department A2-830
BBFO, M/S9

McDonnell Douglas Research
Laboratories
Department 220, Box 516
St. Louis
Missouri 63166
Dr. D. P. Ames

MITRE Corporation
P. O. Box 208
Bedford
Massachusetts 01730
Mr. A. C. Cron

North American Rockwell
Corporation
Autonetics Division
3370 Miraloma Avenue
Anaheim
California 92803
Mr. T. T. Kumagai
C/476 Mail Code HA18

Physical Sciences
Incorporated
Lakeside Office Park
607 North Avenue
Door 18
Wakefield
Massachusetts 01880
Dr. Anthony N. Pirri

Northrop Corporation
3401 West Broadway
Hawthorne
California 90250
Dr. Gerard Hasserjian
Mr. G. R. Wenninger,
Manager Sales System
Laboratories

2

RAND Corporation
1700 Main Street
Santa Monica
California 90406
Dr. Claude R. Culp
Mr. G. A. Carter

Raytheon Company
Foundry Avenue
Waltham
Massachusetts 02154
Dr. Frank A. Horrigan
(Research Division)

Raytheon Company
Bedford Laboratories
Missile Systems Division
Bedford
Massachusetts 01730
Dr. H. A. Mehlhorn
Optical Systems Department
M/S S4-55

Raytheon Company
Boston Post Road
Sudbury
Massachusetts 01776
Dr. Charles Sonnenschien
Equipment Division

	Copies		Copies
Radio Corporation of America Missile and Surface Radar Division Morrestown New Jersey 08057 Mr. J. J. Mayman, Systems Projects		W. J. Schafer Associates, Incorporated Lakeside Office Park 607 North Avenue, Door 14 Wakefield Massachusetts 01880 Francis W. French	
Riverside Research Institute 80 West End Street New York, New York 10023 Dr. L. H. O'Neill Dr. John Bose HPEGL Library	3	Stanford Research Institute 333 Ravenswood Avenue Menlo Park California 94025 Dr. H. E. Lindgerg Mr. J. E. Malick	2
R&D Associates, Incorporated P. O. Box 3580 Santa Monica California 90431 Dr. R. E. LeLevier Dr. R. Hundley	2	Science Applications Incorporated P. O. Box 3507 Albuquerque New Mexico 87110 Dr. John Asmus	
Rockwell International Corporation Electronics Research Division 3370 Miraloma Avenue Anaheim California 92803 Mr. T. T. Kumagai D/528, Mail Code HA14		Science Applications, Incorporated 1701 North Ft. Myer Drive Arlington Virginia 22209 Mr. Lawrence Peckham	
Rockwell International Corporation Rocketdyne Division Albuquerque District Office 3636 Menaul Boulevard, N.E., Suite 211 Albuquerque New Mexico 87110 Mr. C. K. Kraus, Manager		Science Applications, Incorporated P. O. Box 328 Ann Arbor Michigan 48103 Dr. R. E. Meredith	
SANDIA Laboratories P. O. Box 5800 Albuquerque New Mexico 87115 Dr. A. Narath, ORG 5000		Science Applications, Incorporated 6 Preston Court Bedford Massachusetts 01730 Dr. Robert Greenberg	
		Systems Consultants, Incorporated 1050 31st Street, N.W. Washington, D. C. 20007 Mr. Robert E. Ricles	

Copies

Copies

Systems, Science and
Software
P. O. Box 1620
LaJolla, California 92037
Mr. Alan F. Klein

Thiokol Chemical Company
WASATCH Division
P. O. Box 524
Brigham City
Utah 84302
Mr. James E. Hansen

TRW Systems Group
One Space Park
Building 01, Room 1050
Redondo Beach
California 90278
Mr. Norman F. Campbell

United Aircraft Research
Laboratories
400 Main Street
East Hartford,
Connecticut 06108
Mr. G. H. McLafferty
Mr. Albert Angelbeck

United Aircraft Corporation
Pratt and Whitney Aircraft
Division
Florida R&D Center
P. O. Box 2691
West Palm Beach
Florida 33402
Dr. R. A. Schmidtke
Mr. Ed. Pinsley

VARIAN Associated
EIMAC Division
611 Hansen Way
Palo Alto
California 94304
Mr. Jack Quinn

Vought Systems Division
LTV Aerospace Corporation
P. O. Box 5907
Dallas, Texas 75222
Mr. F. G. Simpson
Mail Station 2-54142

Westinghouse Electric
Corporation
Defense and Space Center
Baltimore-Washington
International Airport
P. O. Box 746
Baltimore
Maryland 21203
Mr. W. F. List

Westinghouse Electric
Corporation
Research Laboratory
P. O. Box 10864
Pittsburgh
Pennsylvania 15236
Dr. E. P. Riedel
Mr. R. L. Hundstad

4

3

3

2

SPECIAL DISTRIBUTION LIST
FOR NSWC/WOL/TR 75-53

Dr. J. J. Barrett
Materials Research Center
Allied Chemical Corp.
P. O. Box 1021R
Morristown, New Jersey 07960

Prof. Daniel Bershader
Dept. of Aeronautics and
Astronautics
Stanford University
Stanford, California 94305

Dr. George Bethke
Room L9517
G.E. Space Science Lab.
P. O. Box 8555
Philadelphia, Pennsylvania 19101

Dr. Graham Black
Stanford Research Institute
Menlo Park, California 94025

AFAPL/SFF (Lt. G. E. Bresowar)
Wright-Patterson AFB, Ohio 45433

Mr. Donald L. Champagne
Gas Turbine Engineering
General Electric Company
Schenectady, New York 12345

Major Maurice Clermont
AEDC/DYR
Arnold Air Force Station
Tennessee 37309

Dr. John W. Daiber
Calspan Corporation
4455 Genesee Street
Buffalo, New York 14221

Mr. Lee Dodge
United Aircraft Research Labs.
400 E. Main Street
E. Hartford, Connecticut 06108

Dr. E. Stokes Fishburn
A.R.A.P.
50 Washington Road
Princeton, New Jersey 08540

Dr. W. W. Hunter
Gas Parameters Measurements
Section
Measurements Physics Branch
NASA Langley Research Center
Hampton, Virginia

Prof. Samuel Lederman
Polytechnic Institute of Brooklyn
Graduate Center
Farmingdale, New York

Dr. Donald A. Leonard
AVCO Everett Research Laboratory
2385 Revere Beach Parkway
Everett, Massachusetts 02149

Dr. E. Robert Sch'ldkraut
Director of Research
Block Engineering, Inc.
19 Blackstone Street
Cambridge, Massachusetts 02139

Prof. Robert Goulard, Director
Project SQUID
Jet Propulsion Center
School of Mechanical Engineering
Purdue University
Lafayette, Indiana 47907

Mr. D. L. Hartley
Sandia Laboratories
Organization 8364
Livermore, California

Dr. A. B. Harvey
Naval Research Laboratory
Washington, D. C. 20390

AFAPL/SFF (Dr. W. H. Heiser,
Chief Scientist)
Wright-Patterson AFB, Ohio 45433

Dr. Ronald A. Hill
Sandia Laboratories, Div. 5642
Albuquerque, New Mexico 87115

Dr. Marshall Lapp
General Electric Company
Corporate Research and Development
P. O. Box 8
Schenectady, New York 12301

Dr. J. W. Lewis
ARO Inc. - VKF/ADP
AEDC
Arnold Air Force Station
Tennessee 37389

Dr. Michael Mack
Electromagnetics Laboratory
United Aircraft Research Labs.
E. Hartford, Connecticut 06108

Dr. Harvey Melfi
Environmental and Space Sciences
NASA Langley Research Center
Bldg. 1230, Mail Stop 234
Hampton, Virginia 23365

Mr. Paul Mossey
Measurement Development
Bldg. 301, Mail Drop H-76
Evandale Plant
General Electric Company
Cincinnati, Ohio 45215

ARL/LF(Mr. David Murray)
Wright-Patterson AFB, Ohio 45433

Dr. G. B. Northam
Environmental and Space Sciences
NASA Langley Research Center
Bldg. 1230, Mail Stop 234
Hampton, Virginia 23365

Mr. James R. Patton, Jr.
Office of Naval Research
Power Branch
Code 473
Department of the Navy
Arlington, Virginia 22217

Dr. C. M. Penney
General Electric Company
Corporate Research and Development
P. O. Box 8
Schenectady, New York 12301

Dr. Arthur V. Phelps
JILA Building, Room 800
Joint Institute for Laboratory
Astrophysics
University of Colorado
Boulder, Colorado 80302

Dr. Ralph Roberts
Office of Naval Research
Director, Power Branch
Code 473
Department of the Navy
Arlington, Virginia 22217

Mr. J. A. Salzman
NASA Lewis Research Center
Mail Stop 54-3
21000 Brookpark Road
Cleveland, Ohio 44135

Dr. Robert C. Sepucha
Aerodyne Research, Inc.
Northwest Industrial Park
Burlington, Massachusetts 01803

Dr. Robert Setchell
Sandia Laboratories
Organization 8364
Livermore, California 94550

Mr. J. R. Smith
Sandia Laboratories
Div. 8333
Box 696
Livermore, California 94550

Dr. David A. Stephenson
Physics Department
General Motors Research Laboratories
12 Mile and Mound Road
Warren, Michigan 48090

Dr. Eric Storm
California Institute of Technology
1201 E. California Boulevard
Pasadena, California 91109

Dr. Donald R. White
General Electric Company
Corporate Research and Development
P. O. Box 8
Schenectady, New York 12301

Dr. S. L. Petrie
The Ohio State University
Aero-Astro Research Lab.
Donn Scott Field
Columbus, Ohio

Mr. H. F. Lee
AFFDL/FXN
50 Meg Bldg. - 24C
Wright-Patterson AFB, Ohio 45433

Col. Robert W. Milling
ARL/CC
Building 450
Wright-Patterson AFB, Ohio 45433